

Burned area and surface albedo products: Assessment of change consistency at global scale

Bernardo Mota^{*}, Nadine Gobron, Fabrizio Cappucci, Olivier Morgan

European Commission, Joint Research Centre, Via E. Fermi, 2749, Ispra 21027, VA, Italy



ARTICLE INFO

Keywords:

Burned area
Fire
Surface albedo
Spatio-temporal physical coherency and consistency
Radiative forcing

ABSTRACT

This paper presents a framework for assessing the physical consistency between time-series of several satellite-based surface albedo and burned area products at global scale. The methodology evaluates the level of agreement of temporal change between these two Essential Climate Variables (ECVs) taking into account their uncertainties. Several configurations of surface albedo and burned area products, including the ones from MODIS Collection 6, Copernicus Global Land Service (C-GLS), Climate Change Initiative (CCI) and the GlobAlbedo, were analysed over the 2005–2011 period at $0.05^\circ \times 0.05^\circ$ spatial resolution. The study evaluates the temporal and spatial coherence level in the ECV changes, and explores the product dependency impact on the fire-driven radiative forcings. The main findings indicate that the level of agreement between these two ECVs depends on the product combination but also on the albedo broadband. Whereas both GlobAlbedo and MODIS albedo changes are consistent both temporally and spatially when combined with any burned area product, the C-GLS albedo changes are characterised by lower levels of agreement. The results also indicate that surface albedo and burned area product changes are physically coherent for all biomes except grasslands and croplands, when using the MODIS burned area product. Using different combinations of burned area and surface albedo products, fire-induced radiative forcing estimates at the surface can differ, according to the biome, by 26% to 46%. The proposed framework identifies lack of coherency and consistency between the two ECVs. This novel approach allows us to address cross-ECV compatibility, and as such offers a valuable toolset to users.

1. Introduction

In environmental science and climate change studies, Essential Climate Variables (ECVs) derived from Earth Observation satellites are becoming increasingly relevant (GCOS, 2011, 2016). At the international level, ECVs are now (pre-)operationally produced, delivered to scientists and used in various policy domains (Bojinski et al., 2014). There is therefore a need for the validation of land ECV products in order to provide full uncertainty budgets (Hollmann et al., 2013; Loew et al., 2017; Merchant et al., 2017).

The burned area products are the primary variables of the *Fire Disturbance* ECV. They are often delivered in map format identifying locations affected by fires, usually on a monthly basis. Boschetti et al. (2009) proposed as best practice for validation to compare the global coarse resolution burned area products with reference data derived from two or more higher spatial resolution sensor images. This has been recently done for Moderate Resolution Imaging Spectroradiometer (MODIS) and Visible Infrared Imaging Radiometer Suite (VIIRS) products using Landsat imagery (Boschetti et al., 2016). Padilla et al.

(2014) recommended selecting reference data with a stratified random sampling design to ensure adequate representation among the major land covers and applied this method to compare the accuracy between several global burned area products. These include the recently released Fire Disturbance product developed for the Climate Change Initiative (CCI) (Alonso-Canas and Chuvieco, 2015).

Fires have a strong influence on climate, directly through the release to the atmosphere of aerosols and gases and by lowering the *surface albedo* (Bowman et al., 2009). Surface albedo is a critical parameter in surface energy budget, numerical weather forecast, and general circulation models (Dickinson, 1983). The broadband albedo is computed as the ratio of the surface upwelling to the downward flux of shortwave solar radiation over the upward semi-hemispherical space (Liang et al., 2010) that impacts the input and relocation of solar energy over the Earth's surfaces (Porter et al., 2010; Trenberth et al., 2009). Surface albedo products are often validated through inter-comparisons against other data-sets and ground-based measurements (Chen et al., 2008; Pinty et al., 2011; Cescatti et al., 2012; Wang et al., 2014; Adams et al., 2016; Cappucci and Gobron, 2017).

* Corresponding author.

E-mail address: bernardo.mota@ec.europa.eu (B. Mota).

In this paper we propose a novel framework to check the physical consistency between changes of two land ECVs (burned area and surface albedo). As they are used together for computing the radiative forcing in climate models (Ramaswamy et al., 2001; Jin and Roy, 2005; López-Saldaña et al., 2015), we explore the impact of using different combinations of these ECVs products to estimate radiative forcing. The framework is based on certain physical assumptions regarding fire-driven surface albedo dynamics (Pinty et al., 2000; Govaerts et al., 2002). After a burning event, a decrease of the surface reflectance occurs due to vegetation loss and the deposition of charcoal and ash.

The next section summarises the ECV product datasets used in this study. Section 3 describes the proposed framework's methodology. Section 4 presents the results and Section 5 the discussion and concluding remarks. Detailed mathematical formulations and statistical tests are described in Appendix A.1 and an evaluation of the methods is given in Appendix B.1.

2. Materials

2.1. Global surface albedo

The following global surface albedo data sets were employed: 1) **GlobAlbedo** products based on MEdium Resolution Imaging Spectrometer (MERIS) and SPOT VEGETATION data (Muller et al., 2012), 2) **MCD43C3** collection 6 based on MODIS imagery (Schaaf and Wang, 2015) and 3) Copernicus Global Land Services **C-GLS** product based on SPOT VEGETATION data (Hagolle et al., 2005). Table 1 summarises the main characteristics of each global surface albedo product. Since their spatial and temporal resolution varies, direct comparisons using these products are not possible without post-processing them. For example, the **MCD43C3** product is generated daily at 0.05° whereas **GlobAlbedo** provides monthly composites at both 0.05° and 0.5° and the **C-GLS** for every 10 days at 1 km. To achieve spatial and temporal uniformity between the products, and with the burned area products, these were aggregated. A weighted average based on the uncertainty was applied to the observations within each month and grid-cell to generate monthly grid-cell products at 0.05°. Detailed information on the pre-processing steps can be found in Cappucci and Gobron (2017).

This study uses the Bi-Hemispherical Reflectance (white-sky albedo) in the shortwave (SW) and near-infrared (NIR) broadband domain. For simplicity, this surface albedo will be hereafter referred to as albedo and denoted by ρ . The uncertainties supplied by each albedo product are based on different sources of information, and even though the native retrieval algorithm used a kernel-driven model inversion, these are implemented differently. The **GlobAlbedo** product uncertainty is based on the full error propagation throughout the retrieval algorithm. The uncertainty of the **C-GLS** product is based only on the bidirectional reflectance distribution function (BRDF) fitting error and on the narrow to broadband conversion. The **MCD43C3** product uncertainty is based only on the BRDF error fitting. For the case of the **MCD43C3** and **C-GLS** products, we considered as uncertainty the spatial-temporal standard deviation. A comparative analysis of the derived product uncertainty distributions, at global scale for the entire period, showed that all combinations passed the two-sample Kolmogorov-Smirnov test

($p < 0.05$, on all cases). This ensured that distribution differences are minimal and therefore, compatibility between the product albedo uncertainties was assumed.

2.2. Global burned area

Three global burned area products were used in the study: the Fire Climate Change Initiative, **FCCI**, based on MERIS data (Alonso-Canas and Chuvieco, 2015), the **MCD64A1** product from MODIS (Giglio et al., 2009), and the Copernicus Global Land Services **C-GLS** product, build on SPOT-VGT imagery (Tansey et al., 2008). Although other products (such as GBA 2000 Tansey et al., 2004 and the MCD45A1 Roy et al., 2005) exist, we focused only on existing products that cover multiple years and are currently in operational or pre-operational phase. A summary of the burned area products' characteristics are reported in Table 2.

As burned area products result from pixel-based algorithms, their spatial resolution depends on the sensor imagery, which varies from 300 m to 1 km. In addition, the product temporal resolution differs as indicated in Table 2. For example, the **C-GLS** burned area product is supplied every 10 days whereas we have monthly periodicity for the other burned area products. In order to achieve the common spatial and temporal resolution with the albedo products, the burned area products were aggregated to 0.05° resolution in the form of percentage of burned occurrence. For the case of the **C-GLS** product, monthly maps were created by accumulating 10-day values prior to the spatial aggregation. Burned area percentage within each grid-cell will be hereafter called burned area and denoted a [%].

Burned area detection algorithms are mainly based on optical imagery and highly dependent on the near-infrared spectral band. These can employ different approaches such as: detection of temporal and spatial differences in reflectance (Tansey et al., 2008), combined with other bands through spectral indices (Giglio et al., 2009; Alonso-Canas and Chuvieco, 2015) or divergence with forecast surface reflectance based on a fitted Bidirectional Reflectance Factor model (Roy et al., 2005). Furthermore, certain algorithms rely on thermal information (Giglio et al., 2009; Alonso-Canas and Chuvieco, 2015). This means that all these (pre)operational burned area products have a high dependency on each sensor's near-infrared (NIR) spectral band. It is therefore expected to have a higher level of agreement and consistency between near-infrared broadband albedo and burned area products.

2.3. Global Land Cover

Land Cover (LC) was derived from the Climate Change Initiative Land Cover products using epoch 2010 product (UCL-Geomatics, 2014; Tsendbazar et al., 2016). We performed a spatial aggregation using the majority rule according to the dominant LC class. Only grid-cells for which the dominant LC class exceeds 50% were considered representative, all other grid-cells being discarded from the analysis. The aggregation results were analysed as a function of four vegetation groups denoted by 1) Managed lands and croplands, 2) Trees and Woody, 3) Shrubs and 4) Herbaceous; hereafter referred to as Crop-lands, Forests, Shrubs and Grasslands, respectively. These landcover classes will hereafter be referred to as *biomes* (Fig. 1).

Table 1
Surface albedo product characteristics.

Product name reference	Sensor	Spatial resolution	Temporal resolution and coverage	URL
GlobAlbedo Muller et al. (2012)	MERIS, VGT and AATSR	0.05° 0.5°	Monthly 1998–2011	http://www.globalbedo.org/
MCD43C3 Schaaf and Wang (2015)	MODIS Terra and Aqua	0.05°	Daily 2000–present	https://lpdaac.usgs.gov/
C-GLS Hagolle et al. (2005)	SPOT-VGT 1 and 2	1 km	10 days 1999–2014	http://land.copernicus.eu/global/

Table 2
Burned area products characteristics.

Product name and reference	Sensor	Spatial resolution	Temporal resolution and coverage	URL
Fire CCI v4.1 https://geogra.uah.es/esa/	MERIS	300 m	Monthly 2005–2011	
Alonso-Canas and Chuvieco (2015)				
MCD64A1-C6 ftp://ba1.geog.umd.edu	MODIS Terra	500 m	Monthly 2000–present	
Giglio et al. (2009)				
C-GLS http://land.copernicus.eu/global/	SPOT-VGT and Aqua	1 km	10 day 1999–2014	
Tansey et al. (2008)	1 and 2			

3. Methods

3.1. Framework

The proposed framework is based on physical assumptions regarding fire-driven albedo dynamics (Pinty et al., 2000; Govaerts et al., 2002). Fire consumes vegetation by turning it into charcoal and ash, which leads to a drop in albedo in the NIR broadband. The magnitude of this decrease depends on the type of burned vegetation and the severity of the burn. Following the fire event, ash and charcoal are dispersed revealing bare soil with higher reflectance, leading to an increase in surface albedo. When vegetation starts to recover, the growing vegetation leads to a progressive decrease of albedo. Under the same pre-fire conditions, we assume that within a grid-cell, bigger/smaller fire events should lead to a bigger/smaller drop in the albedo value. Therefore, compatibility between albedo (ρ) and burned area (α) is based on how both variables change (Δ) according to the following conditions:

$$\Delta\alpha \Rightarrow \Delta\rho \quad (1)$$

$$\Delta\alpha > 0 \Rightarrow \Delta\rho < 0 \quad (2)$$

$$|\Delta\alpha_1| > |\Delta\alpha_2| \Rightarrow |\Delta\rho_1| > |\Delta\rho_2| \quad (3)$$

where $\Delta\rho$ is the albedo change, $\Delta\alpha$ is the burned area change, and subscripts 1 and 2 refer to two burned area size events.

The first condition establishes the cause-and-effect, the second depicts the coherent direction of change and the last one, determines the scale between events of different magnitudes.

3.2. Study outline

Two analyses are proposed to assess the consistency of changes between the albedo and burned area products: a change agreement and a magnitude coherency analysis (see Fig. 2).

In the first analysis we evaluate the spatial and temporal consistency of the agreement between simultaneous changes in albedo and burned area for each product combination (Section 3.3). Product changes are classified according to a level of confidence (Section A.1) and agreement and bias indicators (Section A.2) are used to assess trends and identify hot-spot areas of potential product (in)consistency.

In the second analysis we evaluate the significance and coherence in the corresponding magnitudes of change between both ECVs (Section 3.4). The significance is assessed to determine how well albedo changes represent a fire event (Appendix A.3) and coherency is checked between the magnitudes of change in albedo and burned area (Appendix A.4).

3.3. Agreement analysis

The confidence level of a change is derived using the uncertainties associated to each product (see Appendix A.1 for formulation and Appendix A.4 for verification). Since no burned area product uncertainty is provided, we associate 15% in area extent, as suggested in the Fire CCI User Requirement Document (Heil et al., 2016) and described by Mouillet et al. (2014), as the reasonable acceptable uncertainty. Changes in both burned area and albedo are classified by their significance and sign. A 50% confidence level threshold is used to determine if each change is significant, otherwise the change lacks confidence (NC). When considering simultaneous changes that occur in both ECVs, nine possible change classification types can occur. These

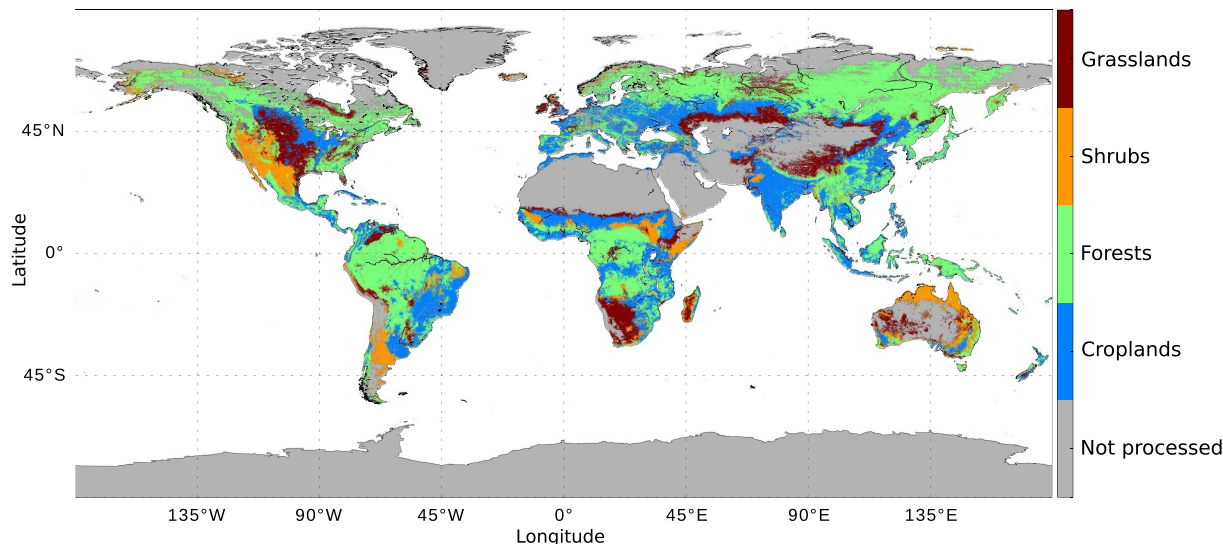


Fig. 1. Spatial distribution of biomes derived from the Land Cover Classification scheme (LCCS), at 0.05° spatial resolution, based on the CCI landcover product (epoch 2010).

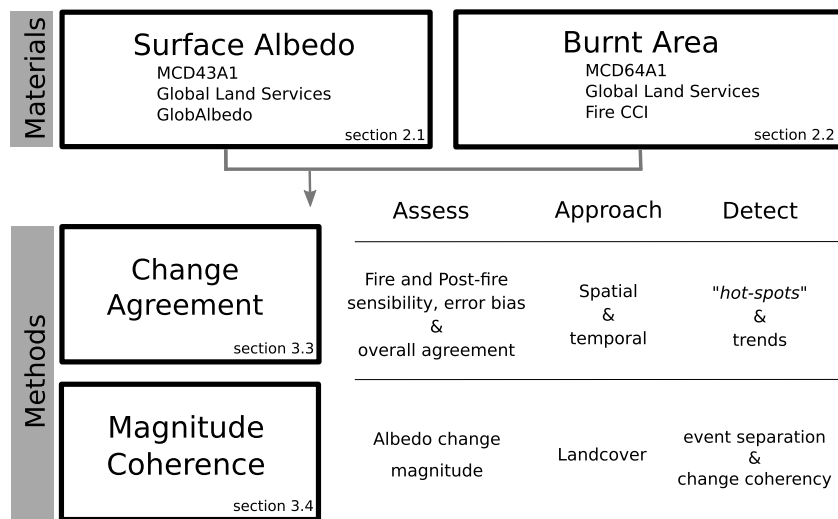


Fig. 2. Flow chart of the analysis.

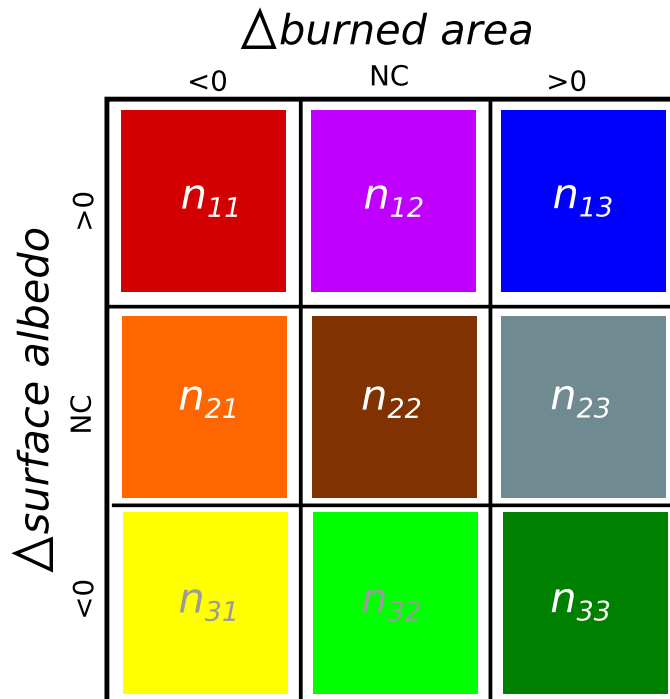


Fig. 3. Contingency table representing the burned area and albedo change classifications based on the significance of change observed simultaneously within each product. Diagonal elements represent coherent cases of fire (n_{33}), post-fire (n_{11}) and no-confidence changes in both products (n_{22}).

can be counted and used to populate the scheme, known as a contingency table, portrayed in Fig. 3.

Physical coherent situations can only assume three cases: 1) a fire-event represented by an increase in burned area and a decrease in albedo (n_{33}), 2) the reverse situation representing post-fire recovery (n_{11}), and 3) cases for which both simultaneously changes (in burned area and albedo) are non-significant (n_{22}). Non coherency is illustrated by the cases where significant burned area increase/decrease leads to a significant albedo increase/decrease (n_{13} and n_{31}), respectively.

The level of agreement is evaluated using statistical metrics developed for classification accuracy (Story and Congalton, 1986). Overall agreement (OA) is determined by the total percentage of coherent change cases represented by the diagonal elements of the contingency

table (Fig. 3) and is given by:

$$OA = 100 \cdot \frac{\sum_{i=1}^3 n_{ii}}{N} \quad (4)$$

where n_{ii} are the number of cases that fall into each change classification type ($i = 1, 2, 3$) and N is the total number of cases.

Omission and commission errors (Janssen and Vanderwel, 1994) are combined into a single metric known as a “dice coefficient” (Dice, 1945; Forbes, 1995) that has a probabilistic interpretation: given that one burned area product identifies an event, the dice coefficient (DC) is equal to the conditional probability that the albedo product is associated with a corresponding coherent change (Fleiss et al., 2013). Its mathematical description and assessment is given in Appendices A.2 and B.2, respectively.

The level of agreement between the changes for each combination of burned area and albedo product is temporarily and spatially analysed. Temporal consistency is based on a map approach where each month, all changes are counted and checked for agreement. A similar approach is used for spatial consistency with a grid-cell approach based on its temporal changes.

3.4. Magnitude coherency

To evaluate the level of consistency between albedo changes and fire events, it is necessary to assess whether their amplitudes match. To ensure that the albedo changes represent a fire-event, we first check if the albedo changes associated with a burned area increase statistically and differ from those associated with a burned area decrease.

Fire events and post-fire events (i.e., vegetation recovery) are defined for each grid-cell according to the observed monthly changes as:

- **Fire events** correspond to cases where burned area increases and where no previous burned area existed, i.e., positive changes requiring an initial condition of no burn:

$$\Delta\alpha > 0, \text{ where } \alpha_{t+1} > 0 \wedge \alpha_t = 0 \quad (5)$$

- **Post-fire events** correspond to cases where a decrease in burned area leads to no further change in burned area, i.e., negative changes requiring a final condition of no burn:

$$\Delta\alpha < 0, \text{ where } \alpha_{t+1} = 0 \wedge \alpha_t > 0 \quad (6)$$

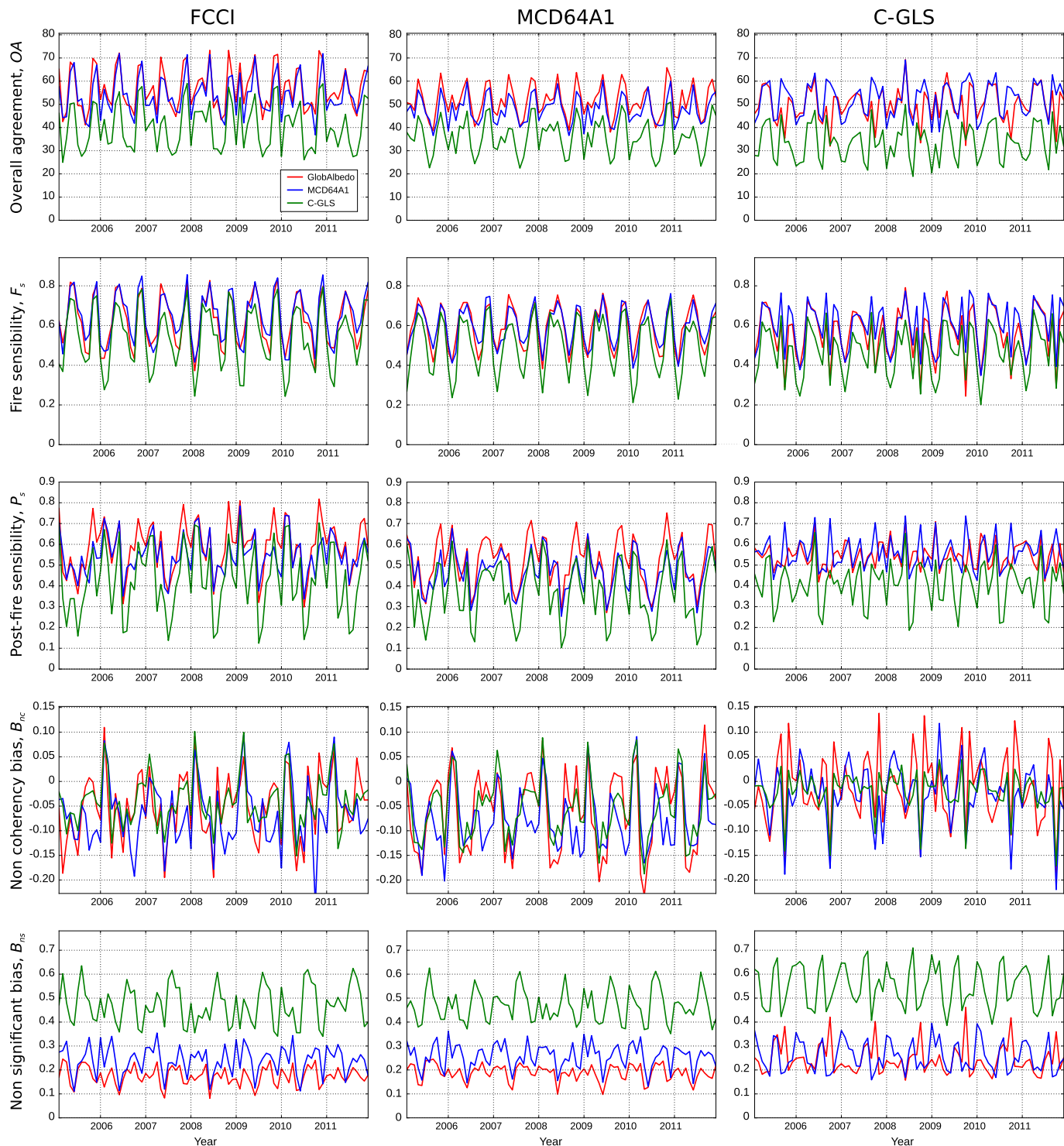


Fig. 4. Temporal profiles of the change agreement metrics (rows) between the simultaneous changes of the near-infrared broadband albedo products (**GlobAlbedo** in red, **MCD43C3** in blue and **CGLS** in green) and the burned area products (columns) at 0.05° spatial resolution from 2005 to 2011. (For interpretation of the references to colour in this figure legend, the reader is referred to the web version of this article.)

These event requirements ensure that only the most unambiguous sets of burned area changes are considered and therefore only clear fire-driven albedo changes are analysed. In addition we calculate the natural seasonal albedo, denoted ‘surrounding’ albedo afterwards, using values over the non-fire affected neighbouring grid-cells. The extent of this area is determined on a monthly basis, and consists of a buffer around the fire affected grid-cells occupying a similar or larger area.

All albedo changes are grouped into corresponding bins of burned

area (α) change magnitude (CM). These bins are defined as a 5% interval in α change, between 0% and 100%, totalling 20 CMs. For each CM, the albedo change distribution, associated with fire and post-fire event, is extracted by biome. For each distribution, both the mean (ξ) and percentage of negative changes of albedo (ϕ) are calculated, representing respectively the mean response and the level of coherency.

Coherency between each albedo and burned area product combination is evaluated according to the following requirements:

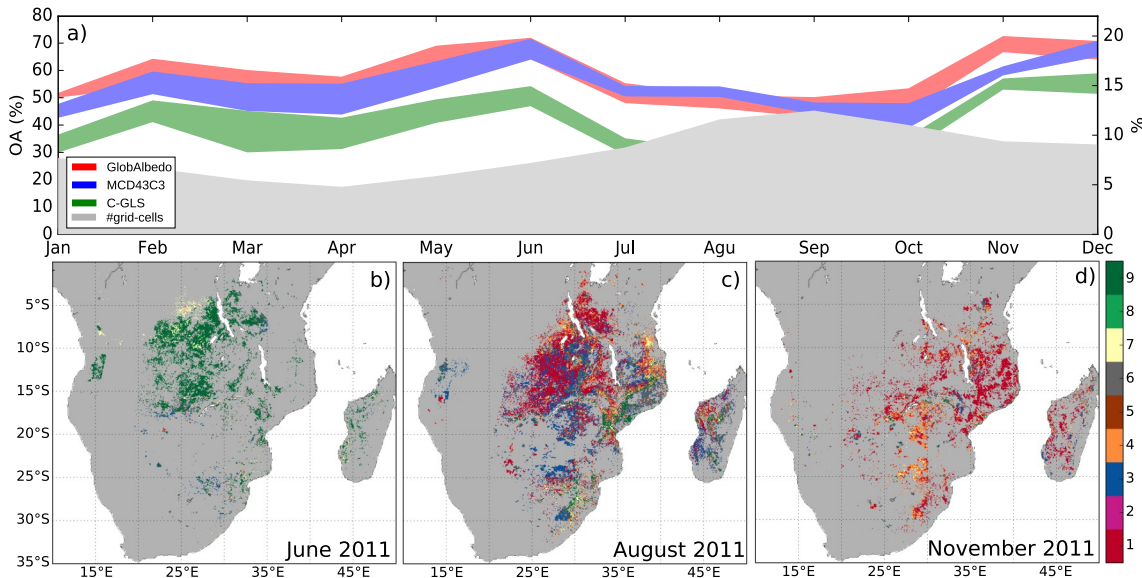


Fig. 5. a) Seasonal profile (2005–2011) of the overall agreement (OA) between the near-infrared broadband of the **GlobAlbedo** (red), **MCD43C3** (blue) and **C-GLS** (green) albedo products, and the CCI burned area product at 0.05° spatial resolution. Shaded areas represent one standard deviation range around the mean. Classified simultaneous changes between Fire CCI burned area product and **GlobAlbedo** product for the near-infrared broadband for b) June, c) August and d) November 2011, at 0.05° spatial resolution over southern Africa. Colour scheme represents the nine change classifications highlighted in Fig. 3. (For interpretation of the references to colour in this figure, the reader is referred to the web version of this article.)

- **Req.1:** Fire and post-fire events are characterised by distinctive and opposing albedo changes,
- **Req.2:** Fire-driven albedo changes should reflect burned area size event in terms of direction and magnitude of change.

To comply with the first requirement, both the sets of mean (ξ) and percentage of negative changes of albedo (ϕ) values are used to assess if separability between fire and post-fire events exists. For the second requirement, only the set of mean changes of albedo is used to assess if larger/smaller burned area changes lead to larger/smaller albedo changes.

Two statistical tests are applied sequentially to evaluate if these requirements are fulfilled. A separation permutation procedure test is first used to evaluate the level of distinction between fire and post-fire event albedo changes. This test is applied using both event statistics (ξ and ϕ). A high level of separability ensures that the albedo changes, associated with burned area increase, are in fact statistically representative of a fire event. In the second test, the coherency in the mean albedo changes is evaluated. For this, a Mann-Kendall trend test is applied to the mean albedo changes (ξ) to check if a significant negative trend exists. Both tests are detailed in Appendices A.3 and A.4, respectively. These procedures are applied to all combinations of albedo and burned area products for each biome, using both the SW and NIR broadband albedo.

3.5. Fire-driven radiative forcing estimates

Ramaswamy et al. (2001) defined the radiative forcing as the change in net (downward minus upward) solar and long-wave irradiance expressed in [W m⁻²]. In this study we consider only the shortwave radiative forcing. When a fire event occurs, the albedo change (Δp) is used to compute the radiative forcing (ΔR_s) at the surface as follows:

$$\Delta R_s = I_{s0}^{\downarrow} \Delta p \quad (7)$$

where I_{s0}^{\downarrow} is the monthly mean downward solar radiation flux at the surface [W m⁻²].

The radiative forcing is calculated using the corresponding downward solar radiation flux measured at the surface for grid-cells in which

fire-driven albedo change occurs (Section 3.4). We use I_{s0}^{\downarrow} provided by European Centre for Medium-Range Weather Forecasts (ECMWF) ERA-interim reanalysis dataset (Dee et al., 2011). The data correspond to monthly means of daily forecast accumulations of surface solar radiation downwards at 0.125° × 0.125° grid cells from 1979 to the present. For the purpose of this study, values are re-sampled at 0.05°.

In order to compare the results for each albedo and burned area product combination, the radiative forcing is spatially aggregated by biome, and temporally averaged for the entire period. Averages are weighted, based on the percentage of burned area in each grid-cell according to:

$$\Delta R_s = \frac{\sum (\Delta R_s \cdot \alpha)}{\sum \alpha} \quad (8)$$

where ΔR_s and α are the radiative forcing and burned area that occur in each grid-cell, respectively. By weighting the average with the burned area we ensure that the contribution from the unburned part within each grid-cell to the albedo change is minimised.

4. Results

4.1. Agreement analysis

The monthly changes in both albedo and burned area for each product combination are classified according to the direction and significance of change as described in Section 3.3 and Appendix A.1. Fig. 4 shows the temporal profiles (2005–2011) of the agreement metrics for product combinations when using the near-infrared broadband albedo. The panels, going from left to right, correspond to FCCI, MCD64A1 and C-GLS burned area products. Each combination with the albedo product is plotted in red, blue and green lines, and represent the **GlobAlbedo**, **MCD43C3** and **C-GLS**, respectively. Row panels, from top to bottom, correspond to the five agreement metrics, i.e., overall agreement (OA), post-fire sensitivity (P_s), fire sensitivity (F_s), non-coherency bias (B_{nc}) and non-significant bias (B_{ns}).

Temporal variations of OA, P_s and F_s for the product combination show, on average, consistent and similar annual patterns with two periods of higher values: from May to June and from November to

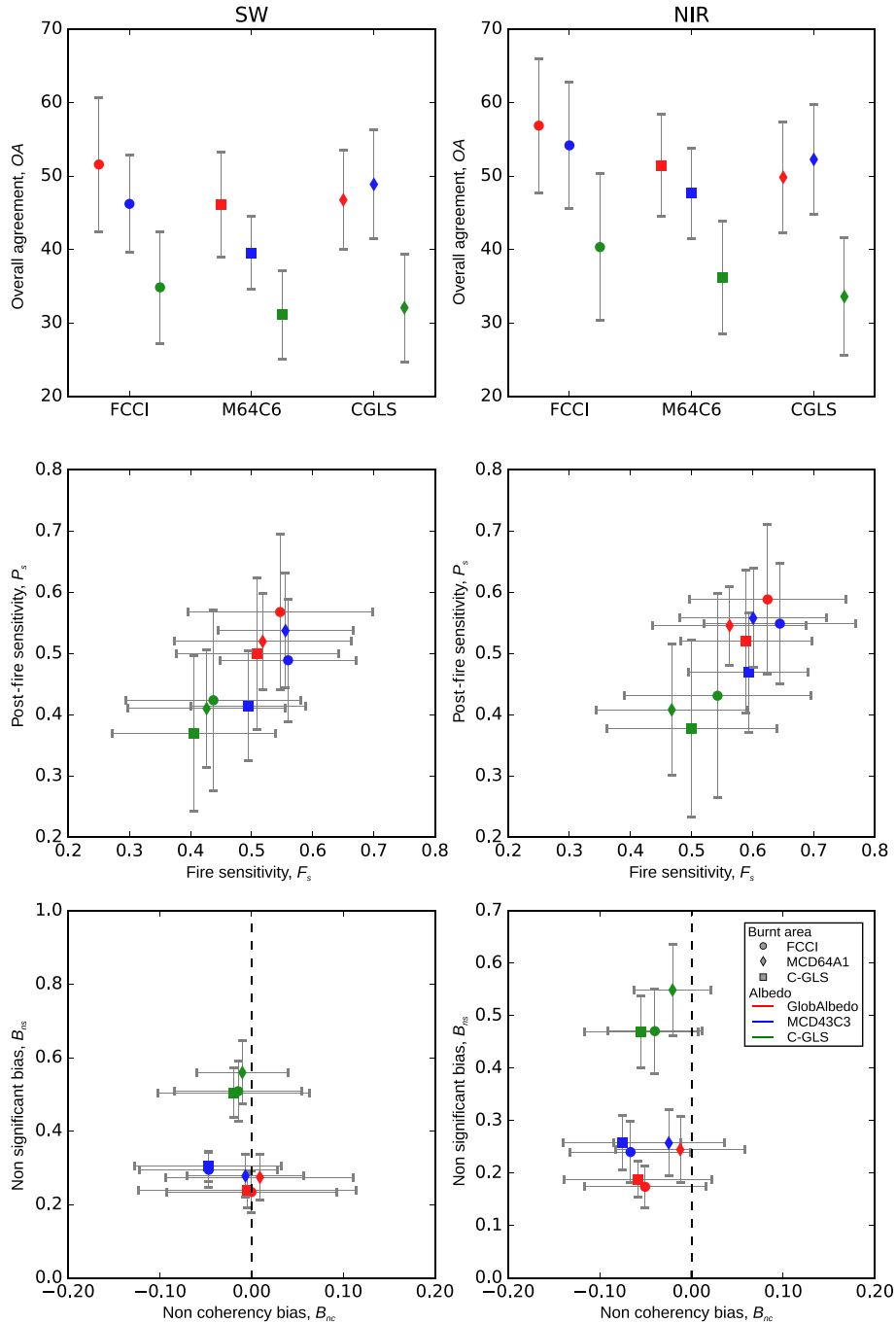


Fig. 6. Temporally averaged (2005–2011) agreement metrics between simultaneous changes observed in the GlobAlbedo (red), MCD43C3 (blue) and CGLS (green) albedo products, for the shortwave broadband (left hand side panels) the near-infrared broadband (right hand side panels), and the FCCI (circle), MCD64A1 (diamond) and C-GLS (square) burned area products at 0.05°. (For interpretation of the references to colour in this figure legend, the reader is referred to the web version of this article.)

December. Whereas OA and F_s share similar peak positions, those for the P_s are shifted by one month and the earlier one has a lower value. The non-coherency bias tends to be negative and is marked by two opposing peaks: one positive in February and a negative one in July. During these months non-coherency is characterised by simultaneous increases and decreases of α and ρ . Regarding the non-significant changes, their bias is always positive for any product combination. This means that the significance associated with burned area changes is always higher than that associated with albedo changes. In addition, large values in B_{ns} always occur during a low OA period.

During the low OA periods, the majority of grid-cells with changes

are located in southern Africa and northern Australia (August–September), and along the Sahel region of northern Africa and southeast Africa (March–April) (not shown). The percentage of non-coherent changes increases and together with non-significant changes represent the majority of cases, resulting in low OA (below 50%).

For example, Fig. 5 shows the typical simultaneous α and ρ change classifications that take place in southern Africa. In June 2011 (Fig. 5b), most changes are classified as a fire event with significant increase in α and with significant decrease of ρ (green areas). In August 2011 (Fig. 5c), post-fire events take place with significant decrease in α together with an increase of ρ (red areas), and also by a large number of

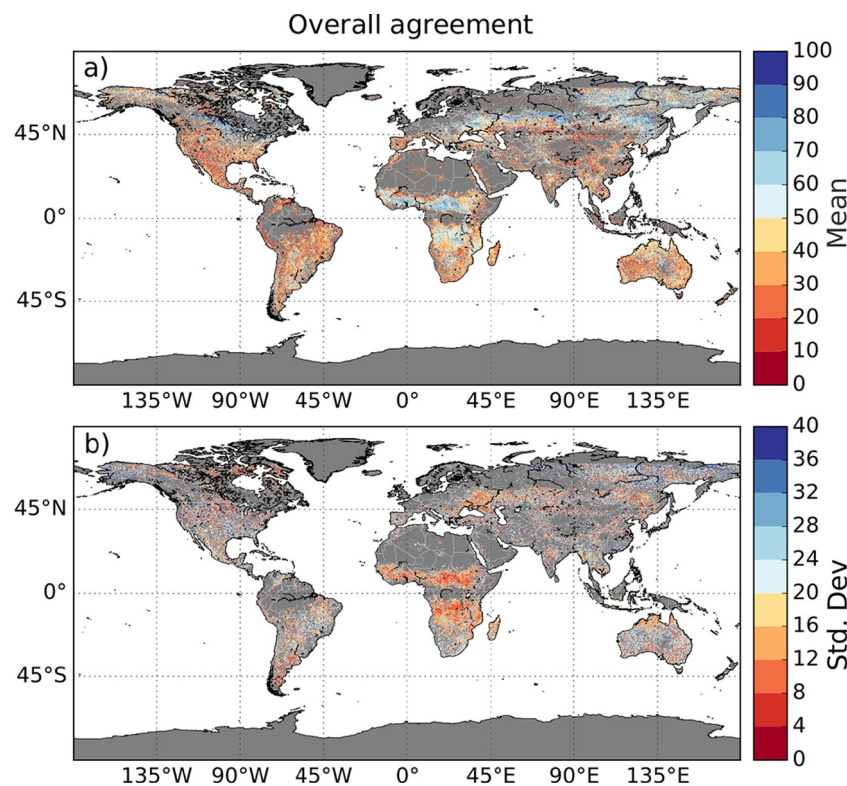


Fig. 7. Spatial distribution of the overall change agreement (OA) for a) the average of the nine possible combinations using the near-infrared broadband albedo products and b) its associated standard deviation, at 0.05° spatial resolution.

non-coherent changes associated with significant decrease of α and ρ (blue areas). These latter non-coherent cases characterise fire events for which the albedo has increased, and therefore contribute to a decrease in OA. Finally, in November 2011 the main changes are associated with significant α decrease, together with significant increase or non-significant changes of ρ , contributing to an increase in OA (Fig. 5d).

Fig. 6 presents the average agreement metric values over the 2005–2011 period, using either the albedo in SW (left hand side panels) and NIR (right hand side panels) broadband. Both albedo broadbands show similar agreements between the ECV product combinations. A minor increase in OA and P_s and a larger increase in F_s and B_{nc} results when using the NIR broadband albedo

In terms of product combinations, the C-GLS albedo results in lower agreement with any burned area products. This is driven by the higher percentage of non-significant albedo changes as seen in the lower panels of Fig. 6 (green symbols). The combination with the highest agreement is between the **GlobAlbedo** and the FCCI burned area products. Similarly, the product combination characterised with the lowest agreement is the one between the two C-GLS ECV products.

The OA spatial average and its standard deviation (between all nine possible product combinations) are displayed in Fig. 7. Higher average values ($> 50\%$) are located over west and central Africa, the Boreal forest belt in north America and Asia, central Europe (Ukraine), central Australia, south of Brazil and the north part of southern Africa (Fig. 7a). Furthermore, all other regions are characterised by high OA standard deviations, with the exception of some regions in Africa and the Boreal belt. This indicates lack of consistency between some of the product combinations and the location of potential hot-spots (Fig. 7b).

Fig. 8 displays detailed maps of OA over southern Africa. From left to right, the panels correspond to the albedo products and, from top to bottom, to the burned area products. Independently of the ECV product combination, the region is characterised by large OA spatial variability. In addition, the results show that OA hinges on the albedo product, with the C-GLS albedo and **GlobAlbedo** products providing the lower and

higher OA values, respectively. The same patchy areas can be found over: North Angola, Zambia, south Democratic Republic of Congo and central Mozambique with higher OA values, and South Africa, north Mozambique and Namibia with lower ones. Areas of non consistent agreement (hot-spots) are, on average, smaller and scattered and located over parts of Tanzania, central Angola and South Africa.

Fig. 9 summarises the averaged agreement values between albedo and burned area changes as a function of biomes over southern Africa. Left (right) hand side panels relate to the shortwave (near-infrared broadband) albedo, and rows correspond to each agreement metric defined in Appendix A.1. These results are similar to the ones presented in the temporal approach (Fig. 6), with respect to spectral bands and product combinations. One can notice that no significant divergence between biomes exists. Nevertheless, higher overall agreement and post-fire sensibility is present over forests. Over grasslands most combinations are characterised by positive B_{nc} , meaning that non-coherency is mainly due to simultaneous increases in α and ρ values. In the NIR broadband, non-coherency bias for grasslands is on average lower and only **MCD64A1** based combinations lack bias.

At global scale (not shown), we found similar results. Product combinations based on **GlobAlbedo** or **MCD43C3** result in relatively smaller differences than those using the C-GLS albedo. As for the temporal agreement profiles, the C-GLS albedo based combinations are characterised by lower OA and larger positive B_{ns} . This disparity between albedo products is mainly due to the larger relative uncertainties associated with the C-GLS albedo product during fire events. As a consequence, for this product the confidence levels (Eq. (A.1)) are lower, leading to albedo changes being classified as non-significant (n_{21} or n_{23}). Global results also show that C-GLS burned area combinations extend over larger areas, notably over the higher latitudes, Australia and South America (not shown). For these areas, the higher agreement is obtained in combination with the **MCD43C3** product.

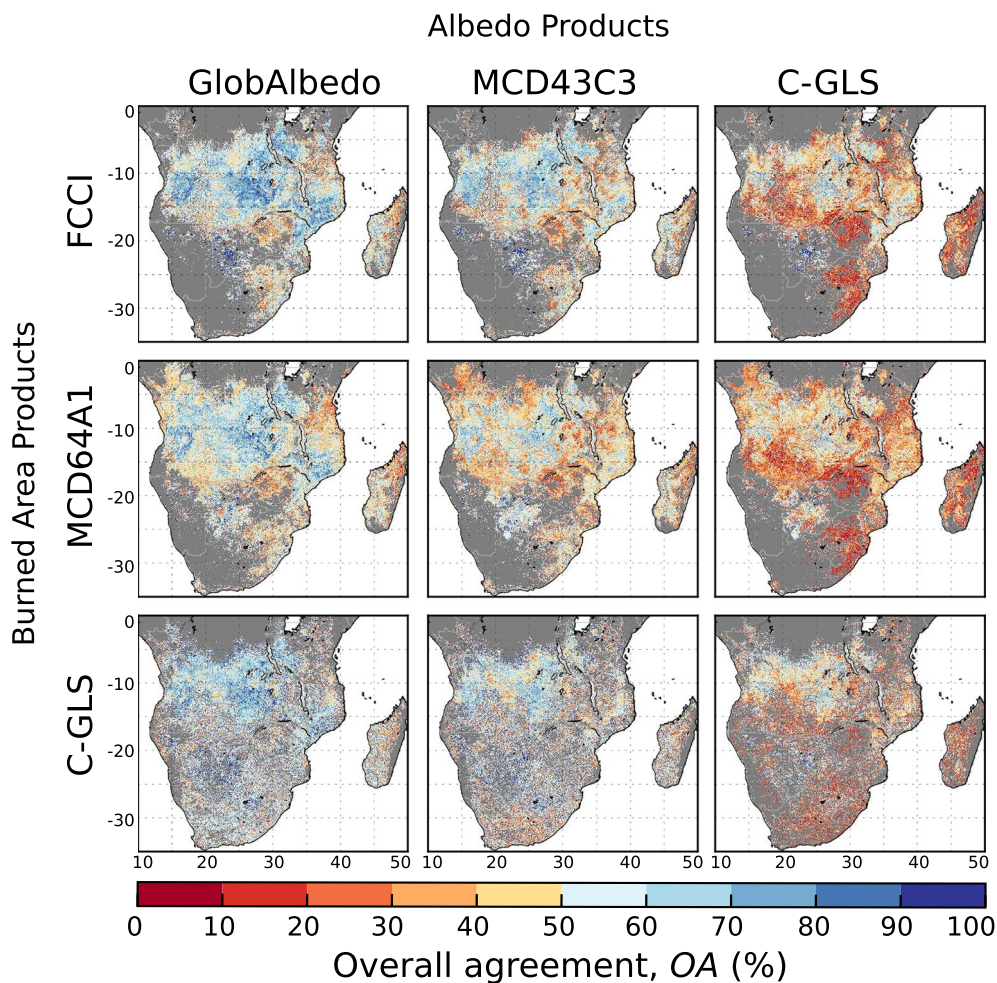


Fig. 8. Spatial distribution of the overall agreement (OA) between near-infrared broadband albedo and burned area products over southern Africa. Horizontal panels relate to albedo products (**GlobAlbedo**, **MCD43C3** and **C-GLS**) and vertical panels to burned area products (**FCCI**, **MCD64A1** and **C-GLS**).

4.2. Magnitude coherency

The S-score tests in Fig. 10 summarise the coherency results of each product combination between burned area and albedo, for the SW (left hand side panels) and NIR (right hand side panels) broadband. Row panels correspond to the FCCI (top), MCD64A1 (middle) and C-GLS (bottom) burned area products, and colours represent their combination with the **GlobAlbedo** (red), **MCD43C3** (blue) and **C-GLS** (green) albedo products. The results show that non coherency, *i.e.*, the lack of a significant negative trend, is restricted to combinations using the **MCD64A1** product. For all other burned area products, independently of the albedo product, a significant negative coherent trend is detected. The results show that using the NIR broadband albedo leads to higher negative scores when compared with the SW albedo one.

Lower negative scores are associated with croplands and forests when using the **C-GLS** or the **FCCI** products. In the case of the **MCD64A1** product, lack of coherence is characterised by positive scores for grasslands and croplands, whilst coherent negative trends over forests are only detected when using NIR broadband albedo products or the **C-GLS** SW broadband albedo. Over shrubs the results always show high coherency between all product combinations.

4.3. Fire-driven radiative forcing estimates

Radiative forcing is computed using monthly shortwave albedo changes for the cases where burned area change increases. Fig. 11 shows the average radiative forcing estimates, weighted by burned grid-

cell extent for each albedo and burned area product combination at 0.05°. Panels indicate the biome and, within each panel, results are aggregated by burned area product (horizontal axis) and blue, red and green colours indicate **GlobAlbedo**, **MCD43C3** and **C-GLS** albedo products, respectively.

One can notice that radiative forcing estimates vary with biome, burned area and albedo product combination. However, within any burned area/biome combination, estimates for each albedo product follow the same ordering pattern: the use of the **GlobAlbedo** provides on average lower estimates whereas the **MCD43C3** product gives higher estimates.

Significantly lower estimates over croplands and grasslands result when using the **MCD64A1** product. Overall, average radiative forcing estimates using all possible product combinations at 0.05° for croplands, forests, shrubs and grassland is 5.25 ± 1.65 , 2.31 ± 0.67 , 2.28 ± 0.60 and 4.68 ± 2.17 (W m^{-2}), respectively. Furthermore, divergence from the mean for each biome ranges from 26% to 46%.

5. Discussion and conclusion

In this paper we focused on the relation between surface albedo and burned area, and its impact to model radiative forcings due to fire induced surface albedo change. We proposed a framework to assess the agreement, consistency and coherence between three global surface albedo and three burned area products based on monthly changes. The method allowed us to identify where, and when, each product combination result is physically (non)coherent. We found divergence between

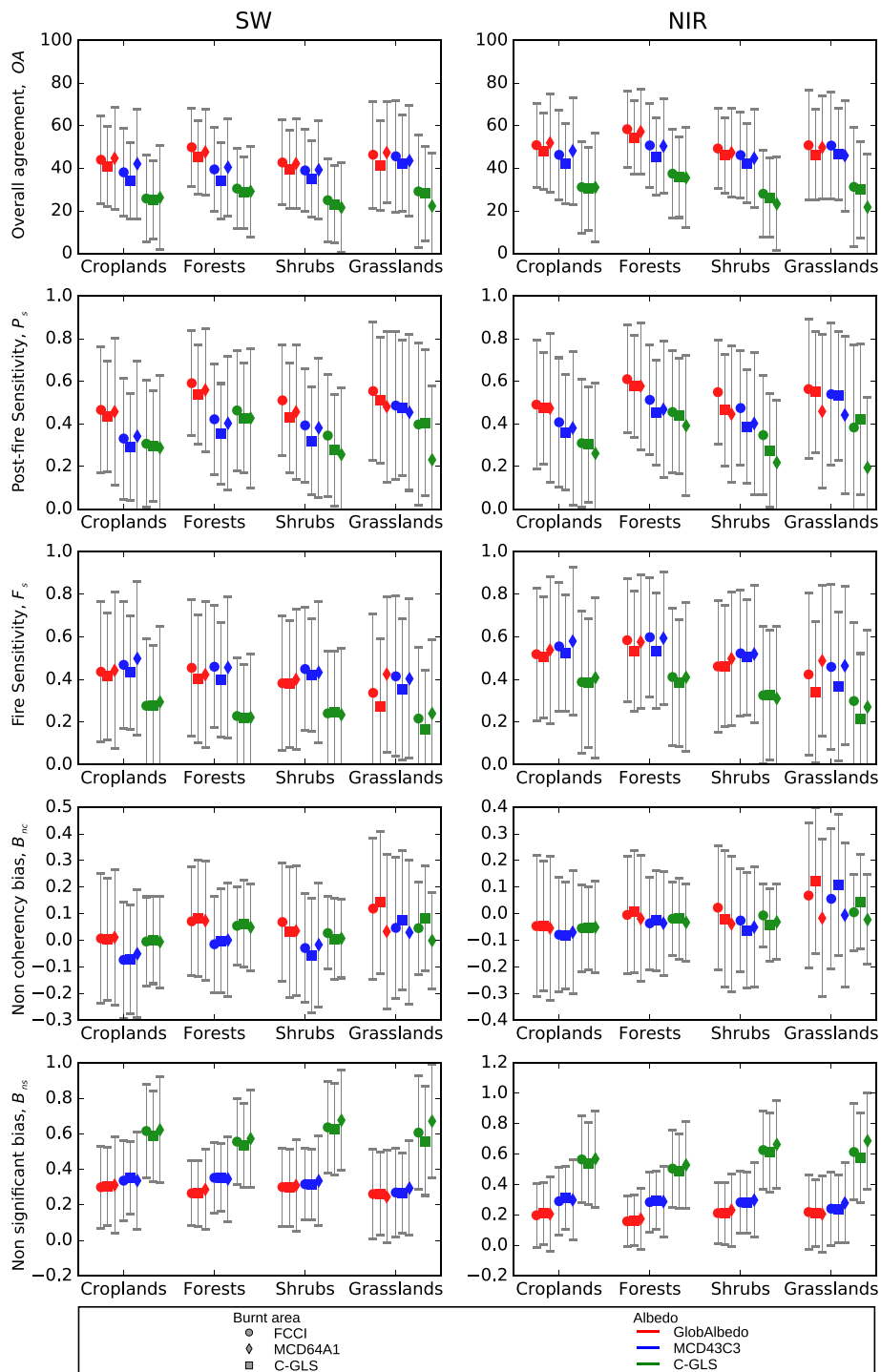


Fig. 9. Change agreement metrics between albedo and burned area products over southern Africa by biome. Symbols represent the spatial average and the associated error bars represent one standard deviation. Left hand side panels relate to the shortwave albedo and right hand panels to the near-infrared broadband. Rows correspond to each agreement metric defined in Appendix A.2.

radiative forcing estimates based on the **MCD43C3** albedo and others products. Although, overall agreement (OA) differences between the **MCD43C3** and **GlobAlbedo** albedo tend to be small, the resulting radiative forcing values differ independently of the burned area product used. This means that for a fire event the albedo perturbation is larger for the **MCD43C3** product compared to the **GlobAlbedo** product. These differences are not only the result of different albedo change magnitudes but also of opposing sign, as shown by the negative non-coherence bias.

The other disparity is the radiative forcing estimates for grasslands and croplands based on the **MCD64A1** product and other burned area products. This difference is linked to a lower coherency in the change magnitudes, indicating that for these vegetation types, **MCD64A1** based changes can agree with the albedo changes in terms of sign, but not in magnitude. There can be many reasons for this and one should not assume that it is necessarily related to accuracy. The probable cause relates to the fact that the **MCD64A1** product algorithm also uses thermal information to revise area estimates. This can lead to

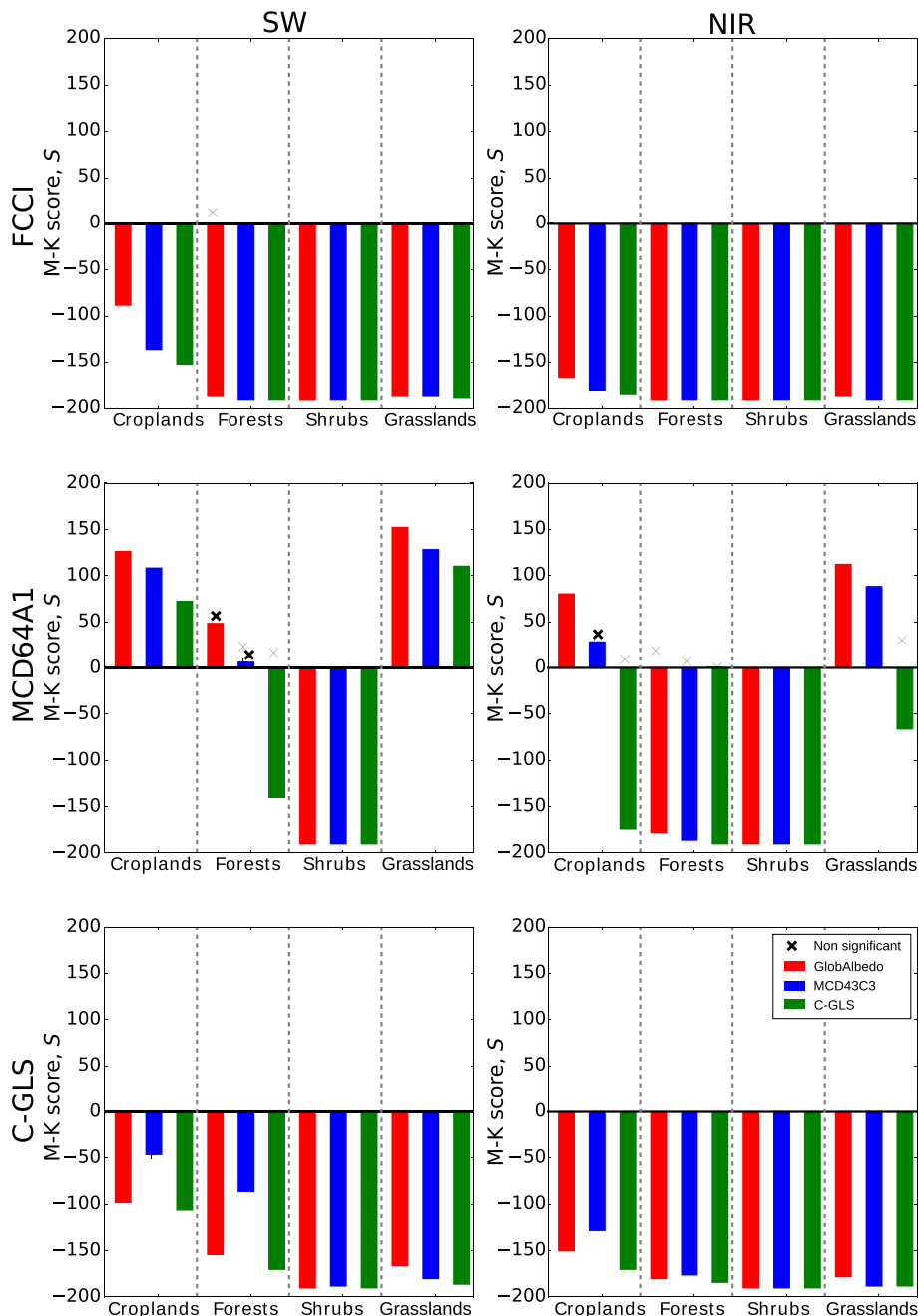


Fig. 10. Trend test S -scores of the albedo change magnitudes, associated with each burned area change size class, by biome in the shortwave (left hand side panels) and near-infrared (right hand side panels) broadbands at 0.05° . A Mann-Kendall non-parametric test is used to evaluate each albedo (GlobAlbedo, MCD43C3, C-GLS) and burned area (FCCI, MCD64A1, C-GLS) product combination. Cross symbols stand for test rejection, i.e. a non-significant trend. (For interpretation of the references to colour in this figure legend, the reader is referred to the web version of this article.)

classification of areas for which the surface reflection changes are not as significant but are supported by thermal detections.

Although radiative forcing estimates based on combinations using C-GLC products (albedo or burned area) are within the range of the other product combination estimates, the proposed framework allows us to identify certain limitations. Compared to the other albedo products (GlobAlbedo and MCD43C3), the C-GLC albedo based combinations are characterised by significantly lower (temporal and spatial) agreements independently of the burned area. This is due to the C-GLS albedo product having larger uncertainties associated with the fire events. This increases the probability of monthly changes being classified as non-significant.

The results indicate that the near-infrared broadband albedo

products reflect better the changes in burned area than the shortwave broadband. This is consistent with the given pertinence by burned area detection algorithm of using near-infrared imagery (Alonso-Canas and Chuvieco, 2015; Giglio et al., 2009; Roy et al., 2005; Tansey et al., 2008). This is evidenced by the lower temporal and spatial agreement scores for the SW but also in the coherence analysis results. In these, the albedo change magnitudes are less representative of the corresponding fire event magnitudes. However, during a fire event the albedo perturbation in the SW broadband reflects burned area changes and therefore could be used to estimate the fire driven albedo radiative forcing effect.

Spatial and temporal resolution may be a limiting factor to assess the coherency and agreement between ECV changes. In the case of the

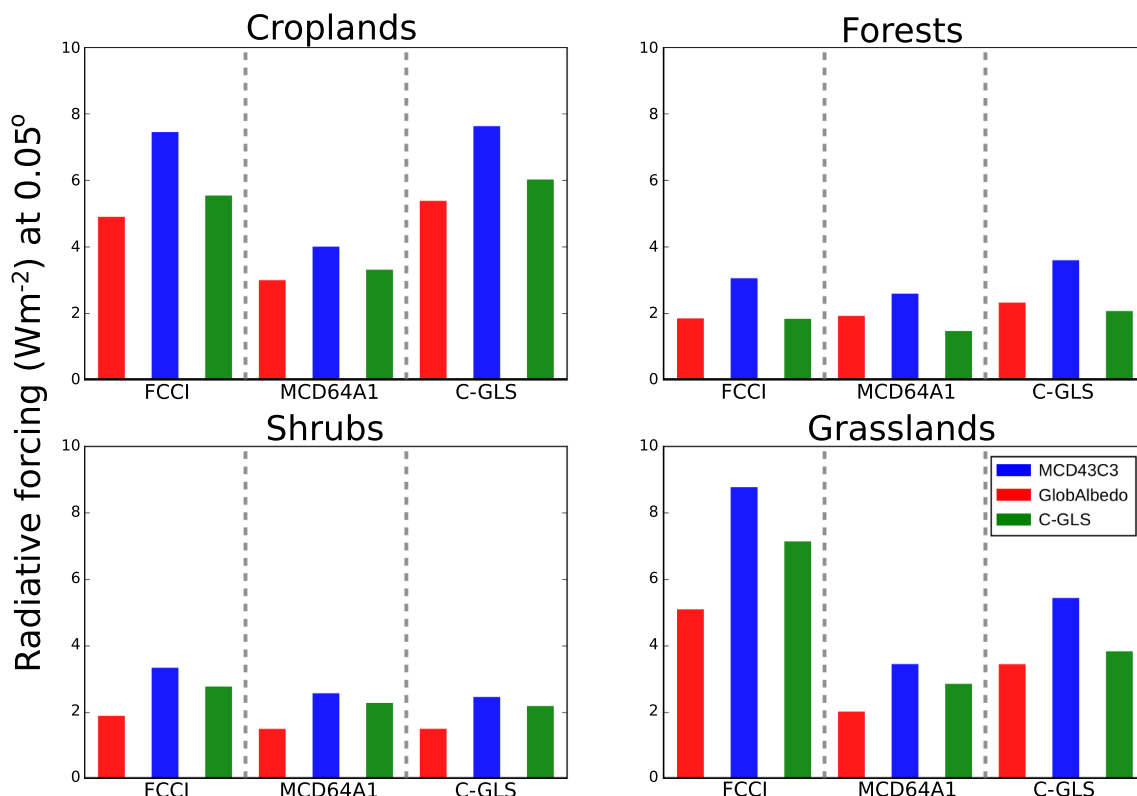


Fig. 11. Radiative forcing estimates induced by fire driven albedo change occurring between 2005 and 2011. These are aggregated by biome (panels) For each albedo (coloured bars) and burned area (x-axis) product combination. (For interpretation of the references to colour in this figure legend, the reader is referred to the web version of this article.)

burned area and surface albedo, at aggregated spatial resolution, the degree to which the fire effect dominates over the background is related to the extent of burned area, the pre-existent vegetation albedo and the severity of the fire event. A small burned area, or one with pre-existent dark vegetation, or a mild burn, contributes less to a change in the albedo than a large burn area, or a severely burned surface or one with pre-existent bright vegetation. The fire signal can be “lost” within the background in coarser resolution grid-cells. In addition, a one month temporal resolution can be long enough for charcoal to be dispersed and reveal a brighter soil (Ward et al., 2012). Lower spatial and temporal resolutions can result in low agreement and lack of coherence, leading to miss-interpretation. Product changes compatibility for low fuel load or small size fire should be conducted at lower temporal and spatial resolutions. Although not ideal, radiative forcing estimates at 0.05° are consistent with other studies derived at higher resolutions (López-Saldaña et al., 2015; Jin and Roy, 2005).

In this study we set the change confidence level threshold to 50%. Imposing a higher threshold could result in a decrease in the number of non-coherent changes, as they would be reclassified as non-significant (as shown in Appendix B.1). However, it would also decrease the number of coherent changes and therefore lower the overall agreement between the ECV product's changes. The opposite effect can also occur when lowering the threshold.

The observed variability in estimates for radiative forcing using different combinations of albedo and burned area products is significant and cannot be ignored. The proposed framework can provide a better understanding of the ensemble uncertainty and also help users select suitable products. In this study the higher overall compatibility is

between the FCCl and **GlobAlbedo** products. A model using any two ECVs, for which there is a known cause-and-effect relation, and displaying a similar ensemble variability, suggests a results dependency on the products used. Therefore, this novel framework can easily be adapted to other suitable ECVs to identify potential non-coherencies and evaluate the consistency between their cross-ECV products.

Fitness for purpose of the available ECV products is not only important in context of product validation but also in terms of cross-ECV compatibility. This paper is an initial effort to address the complexities inherent to multi-product use, and as such offers a valuable assessment tool to users.

Acknowledgments

The support provided by DG GROW, i.e. the European Commission Directorate General for Internal Market, Industry, Entrepreneurship and SMEs, and Copernicus Programme is gratefully acknowledged. The MCD43C3 product was retrieved from the online Data Pool, courtesy of the NASA EOSDIS Land Processes Distributed Active Archive Center (LP DAAC), USGS/Earth Resources Observation and Science (EROS) Center, Sioux Falls, South Dakota. We acknowledge the ESA Climate Change Initiative (CCI) and in particular the Fire disturbance and LandCover projects for supplying the CCI burned area product available at <http://www.esa-fire-cci.org/> and Landcover product available at <http://www.esa-landcover-cci.org>. The MCD64A1 product was retrieved from the University of Maryland at <http://modis-fire.umd.edu>. The authors thank the reviewers for their comments.

Appendix A. Mathematical formulations

A.1. Confidence level

In order to assess the level of agreement between the changes of the burned area and the corresponding albedo, we analyse their mutual occurrences using Eqs. (1) and (2) in [Section 3.1](#). In addition, the significance of a change is also considered by calculating its level of confidence based on each product's uncertainty.

We assume that uncertainties are representative of the standard deviation of a gaussian distribution, centred around each associated observation. The confidence level (C_f) of each temporal change ($t \rightarrow t+1$) is based on the distribution overlap between successive observations. The C_f corresponds to the ratio between the intersecting and the total area occupied by the distributions (see [Fig. A.12](#)). The C_f of a temporal change is given by:

$$C_f|_{t,t+1} = \int_0^1 \frac{|p_t(x) - p_{t+1}(x)|}{p_t(x) + p_{t+1}(x)} dx \quad (\text{A.1})$$

where $p_t(x)$ and $p_{t+1}(x)$ are the probability distribution functions at t and $t+1$, given by:

$$p(x) = \frac{1}{\sigma\sqrt{2\pi}} e^{-(x-\mu)^2/2\sigma^2} \quad (\text{A.2})$$

where μ and σ are the observed and uncertainty values, respectively.

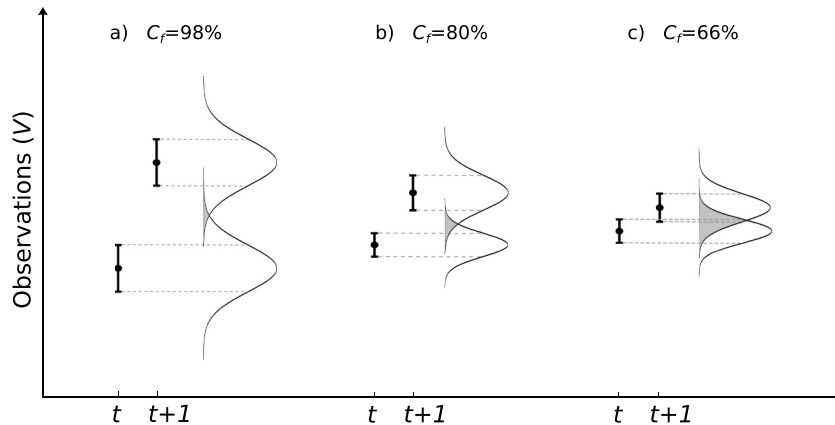


Fig. A.12. Change confidence level at a) 98%, b) 80% and c) 66%. Change confidence level is based on the distributions overlap area (in grey) between two observations. Normal shape distribution is assumed where mean and standard deviation are given by the observation values and uncertainties.

This setting allows us to evaluate the significance of a change, even in cases where the ranges of values (observations bounded by the uncertainty) do not overlap (as in [Fig. A.12a](#) and b). The bigger the distribution overlap, the lower the confidence level of the change. For example, [Fig. A.12a](#) illustrates a large change with a very small overlap and therefore indicates a confidence level close to 100%. For a smaller change, the overlap is larger and therefore results in a lower confidence level ([Fig. A.12b](#)). Even if the ranges of values (represented by error bars) of the two observations barely overlap, the confidence level can be as low as 66% due simply to the distribution tails overlapping ([Fig. A.12c](#)). A confidence level of 100% requires a large change between observations with small associated uncertainties.

A.2. Dice coefficients and error biases

The dice coefficients are hereafter referred to as, fire sensitivity (F_s) and post-fire sensitivity (P_s), given by: and

$$F_s = \frac{2 \cdot n_{11}}{2 \cdot n_{11} + n_{12} + n_{13} + n_{21} + n_{31}} \quad (\text{A.3})$$

$$P_s = \frac{2 \cdot n_{33}}{2 \cdot n_{33} + n_{32} + n_{31} + n_{23} + n_{13}} \quad (\text{A.4})$$

where n_{ij} are the number of cases that fall into each change classification type ($i,j = 1,2,3$) as in [Fig. 3](#) ([Section 3.3](#)).

In addition, the bias related to the frequency of non coherent and non confident changes is evaluated. The non-coherency bias (B_{nc}) accounts for the number of cases where simultaneous increases of burned area and albedo dominate over the number of cases where simultaneous burned area and albedo decreases, and is given by:

$$B_{nc} = \frac{n_{13} - n_{31}}{N} \quad (\text{A.5})$$

Non-significant bias (B_{ns}) highlights the balance in the number of non significant change cases between both products.

$$B_{ns} = \frac{(n_{21} + n_{23}) - (n_{12} + n_{32})}{N} \quad (\text{A.6})$$

A.3. Fire and post-fire separability

The separability between fire and post-fire event albedo changes is tested using a permutation procedure. This procedure is a data-dependent

method for analysing grouped data based on Euclidian distance without any assumption on distribution type (Biondini et al., 1991). The Multi-Response Permutation Procedure (MRPP) method developed by Mielke (1986) is used to evaluate the separability (Fig. A.13). This MRPP method for multivariate analysis, within the BLOSSOM software (Cade and Richards, 2005), is applied to paired data - mean albedo change (ξ) and percentage of negative changes of albedo (ϕ) - associated to each bin of burned area change magnitude (CM).

The hypothesis test states that there is no difference between the fire event and that of the post fire and is given by:

$$H_0: F(\xi_i, \phi_j) = P(\xi_i, \phi_j), \quad \forall i, \forall j \quad \text{versus} \quad H_a: F(\xi_i, \phi_j) \neq P(\xi_i, \phi_j) \quad \text{for some } i, j \quad (\text{A.7})$$

where $F(\xi_i, \phi_j)$ and $P(\xi_i, \phi_j)$ are the two event group sets of ξ_i and ϕ_j ($i, j = 1, \dots, 20$) associated with the CMs.

In principle, fire events are characterised by distributions of negative means of albedo change ($\xi < 0$) and low percentage of positive changes of albedo ($\phi > 0$). Post-fire events should be characterised by distributions of positive means ($\xi > 0$) and high percentages of positive changes of albedo ($\phi > 0$). If these characteristics are verified, the albedo changes that characterise both events are distinctive (Fig. A.13a). If the null hypothesis is not rejected (at $p - val > 0.05$), the two event groups are characterised by low separation (Fig. A.13b), and therefore one cannot assume that the set of albedo changes associated with burned area increase is representative of fire events.

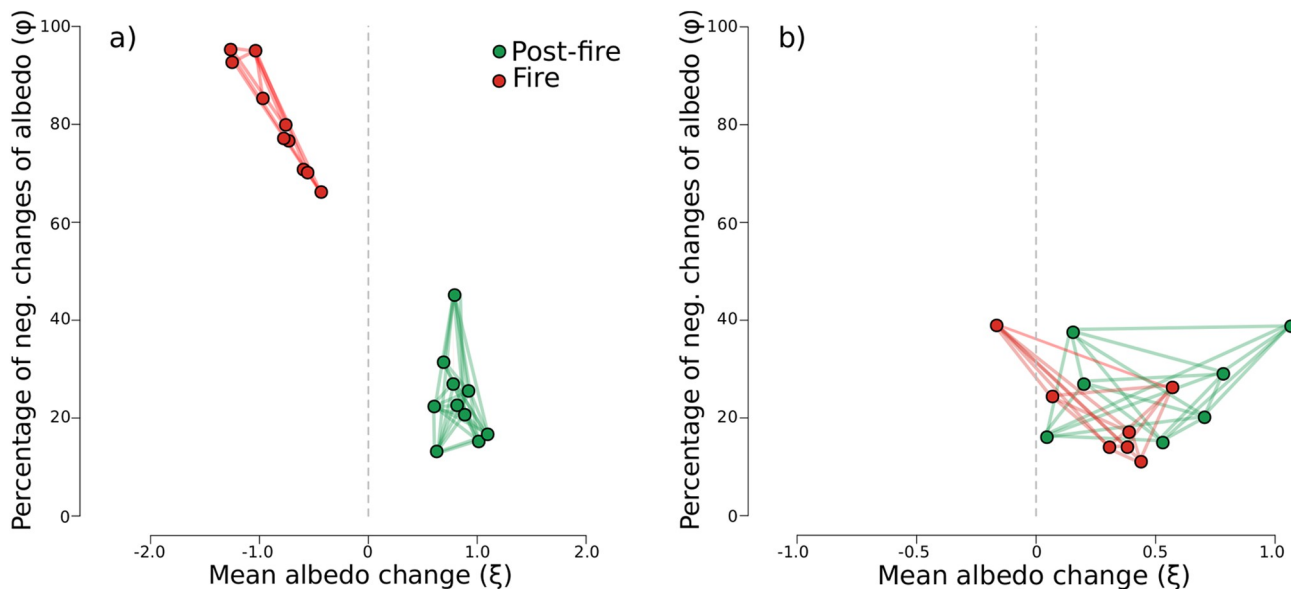


Fig. A.13. Examples of mean (ξ) and percentage of negative changes of albedo (ϕ) at various burned area change magnitude classes for which changes associated with fire (red points) and post-fire (green points) events are a) separable and b) not separable.

A.4. Fire driven albedo change coherency

The coherency between albedo and burned area change magnitudes for fire events is evaluated by performing a trend analysis on the distribution of the mean albedo changes (ξ). Note that this test is only performed with fire events, as post-fire event albedo can require a longer period to change.

The existence of a significant negative trend conforms with condition (3) (Section 3.1) and indicates that, on average, there is coherency in terms of magnitude between the albedo and burned area changes. This can only occur if the smaller albedo decreases are associated with low burned area change magnitude bins (CM), and larger albedo decreases are associated with high CMs. If this relationship is consistent throughout all CM classes, a clear and significant negative trend can be detected.

Due to the unknown function characterising albedo change as a function of burned area change, we select a non-parametric trend test to evaluate the existence and significance of a trend *i.e.* the Mann-Kendall (MK) test (Mann, 1945). In our study, time is replaced by change magnitude (CM) where the initial observation corresponds to the mean albedo of surrounding unburned area.

The MK test score, S , is calculated by:

$$S = \sum_{k=1}^{n-1} \sum_{j=k+1}^n \text{sgn}(\xi_i - \xi_k) \quad (\text{A.8})$$

where ξ_1, \dots, ξ_n are n samples of mean albedo change ranked by each CM.

Appendix B. Assessment of the methodology

B.1. Confidence level and change classification

We demonstrate here the validation of the confidence level approach for change classification by showing first the impact of using different threshold values.

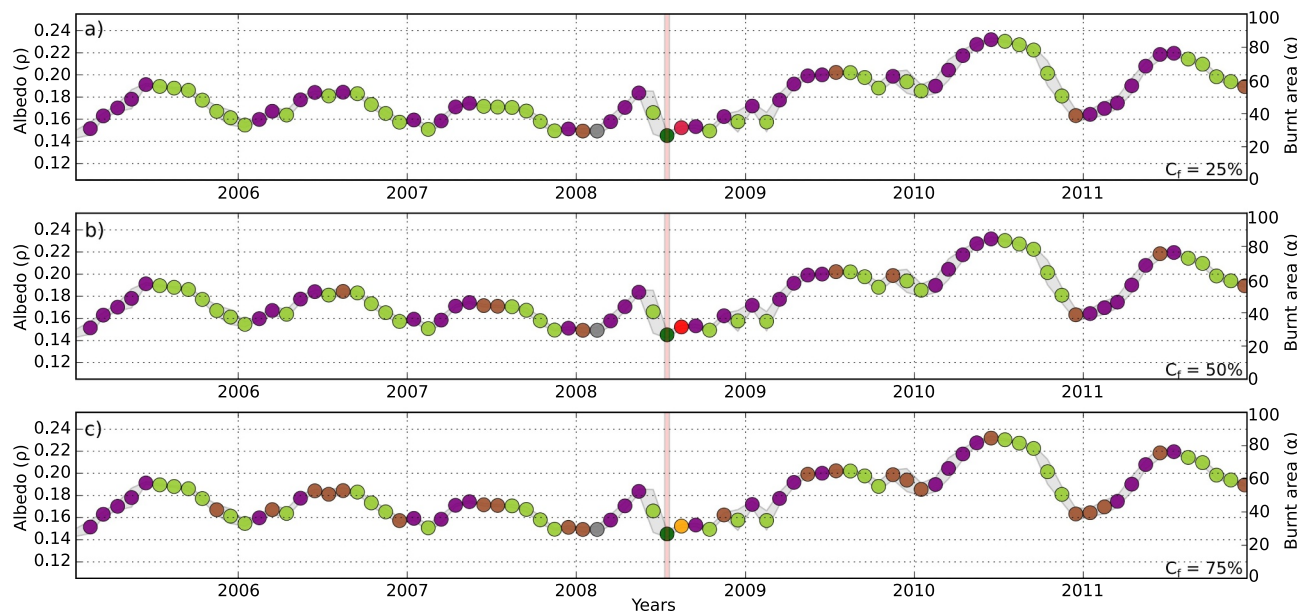


Fig. B.14. Near Infrared broadband albedo (GlobAlbedo) temporal profiles (2005–2011) for a grid-cell located over forest in southern California (37.55°N ; 119.98°W), USA, classified according to the simultaneous changes in burned area (MCD64A1) by applying a) 25%, b) 50% and c) 75% confidence level threshold. The colour scale is consistent with Fig. 3, indicating if simultaneous changes are coherent (red and dark green), incoherent (yellow and blue) or non-significant (brown, magenta, grey, orange). The vertical pink line indicates the burned area event.

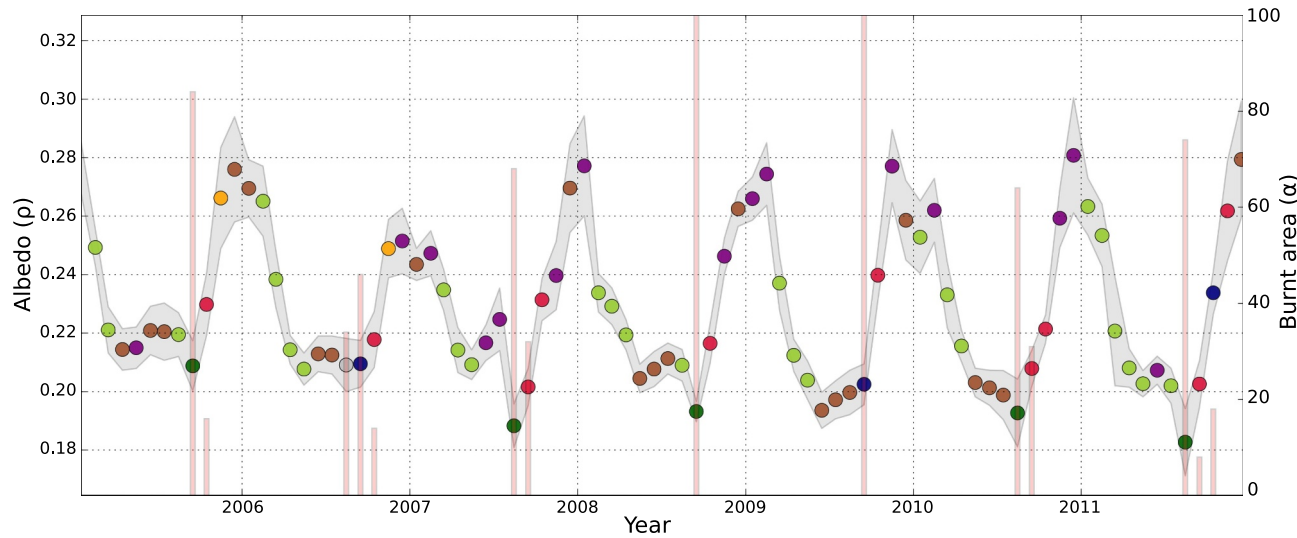


Fig. B.15. Near-infrared broadband albedo (C-GLS) temporal profile (2005–2011) for a grid-cell located over agriculture land in western Zambia (16.55°S ; 23.75°E), classified according to the simultaneous changes in burned area (MCD64A1) by applying 50% confidence level threshold. The adapted colour scheme is consistent with Fig. 3, indicating if simultaneous changes were coherent (red and dark green), incoherent (yellow and blue) or non-significant (brown, magenta, grey, orange). The vertical pink lines indicate the burned area events.

Fig. B.14 presents one example over a forest area located in southern California (37.55°N ; 119.98°W) using the near-infrared GlobAlbedo and the MCD64A1 burned area products. The left (right) y-axis are the albedo (burned area) values. Note that only one fire is detected in August 2008 (pink vertical line). The classification of each change is represented by colours consistent with the ones in Fig. 3 using different confidence thresholds: 25% (top panel), 50% (middle panel) and 75% (bottom panel). Most of the simultaneous changes that occur during the period are classified as non-significant (light green or magenta). The exceptions are the observations between July and August 2008 related to burned activity. In these cases, the fire event is always detected (dark green) for the 3 values of confidence level. It is followed by either post-fire recovery (red) in case of $C_f = 25\%$ and 50% or by a non-significant albedo change (orange) for $C_f = 75\%$. This shows that higher confidence threshold (bottom panel) leads to higher probability of the albedo change being classified as non-significant.

Forest fires tend to be characterised by a significant drop in the NIR broadband albedo and therefore easily classified as coherent. Fig. B.15 shows a second example over an agricultural site located in southern Africa (16.55°S ; 23.75°E) with seasonal fire events occurring every year. Most fires are correctly classified, using the C-GLS albedo and the MCD64A1 burned area product (dark green symbols). However, for some years, as in 2006 and 2009, these simultaneous changes are classified as non-coherent. In these cases albedo increased instead of the expected coherent decrease (blue points).

B.2. Agreement metrics

The applicability of the agreement metrics between albedo and burned area changes is outlined through an example using actual data. Fig. B.16 displays the time series of albedo values from **GlobalAlbedo** (top panel), **MCD43C3** (middle panel) and **C-GLS** (lower panel) together with fire events from **MCD64A1** located over grasslands in northern Australia (13.50°S ; 133.75°E).

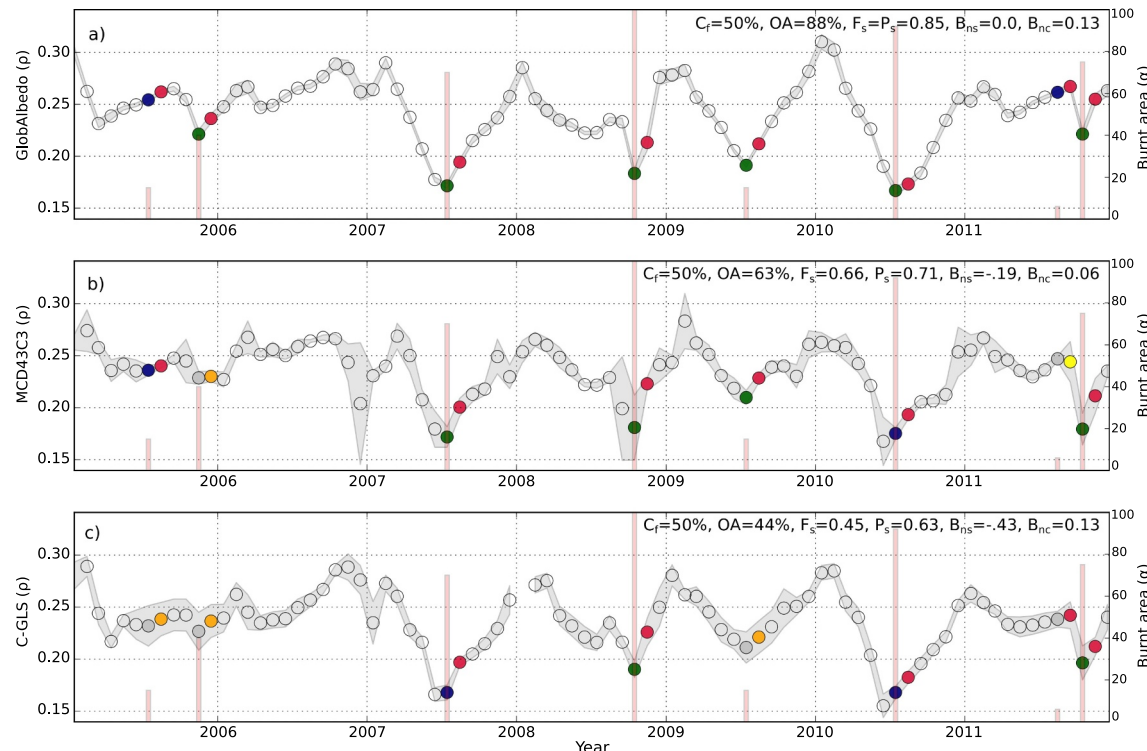


Fig. B.16. Near-infrared broadband albedo temporal profiles (2005–2011) located over grasslands in northern Australia (13.50°S ; 133.75°E), classified according to the simultaneous changes in burned area (**MCD64A1**) and a) **GlobAlbedo**, b) **MCD43C3** and c) **C-GLS** albedo by applying a 50% confidence level threshold. The colour scheme is consistent with Fig. 3 and is only adopted to fire related changes, indicating if simultaneous changes are coherent (green and red), non-coherent (blue and yellow) and non-significant (grey and orange). The vertical pink lines indicate the burned area events.

The values of all agreement metrics are reported in each panel: **GlobalAlbedo** is the product that shows the largest agreement with the **MCD64A1** burned area product ($OA = 88\%$ Fig. B.16a). During this seven-year period, 6 out of 8 fire event changes (fire and post-fire) are classified as coherent. In contrast, the product combination with the lowest level of agreement is the one associated with the **C-GLS albedo** ($OA = 44\%$, Fig. B.16c), where only 2 out of 8 fire changes are classified as coherent. In addition, for the latter case, post-fire sensibility is higher than for fire because more coherent changes occur for post-fires (red) than for fire (dark green) events. This misclassification is due either to the lack of confidence in the changes or to the time lag between burned area and albedo products (as occur during 2007 and 2010). Because one fire is a single temporal event that leads to a significant change in burned area, the non-significant bias tends to be positive, or zero as in the **GlobalAlbedo** example. All products share here the same positive non-coherent bias because all non-coherence classifications are associated with the fire and none with post-fire events.

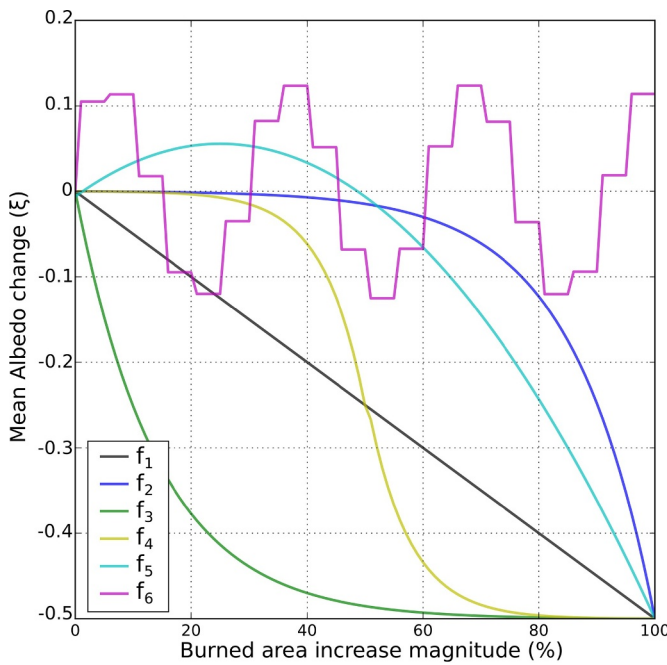


Fig. B.17. Mean albedo change as a function of burned area increase simulations. The functions based on a linear (black), exponential (blue), logarithmic (green) and S-shape curve (yellow) correspond to cases where albedo can only decrease, the parabola (cyan) allows for a small increase of albedo during the low magnitude fire events and the step-like sinusoidal (magenta) representing a function with high variability but with no trend in the mean albedo changes.

B.3. Magnitude coherence

This section addresses the evaluation of the coherency method associated with the fire driven albedo change. In accordance with condition (3) (Section 3), the mean albedo change associated with a fire event class magnitude, should be lower (larger in absolute value) for the larger fire event magnitudes. Here we analyse the results of the method by considering six possible functions reflecting this type of relation: four that follow this condition between all class magnitudes and two that allow for an increase in some of the fire magnitude classes (Fig. B.17).

- The linear function (f_1), whereby the same amount of albedo decrease is observed throughout all fire class magnitudes.
- The exponential (f_2)(logarithm (f_3)) that indicates the cases for which the mean albedo decrease is smaller(bigger) for the lower class magnitudes and larger(smaller) to the higher class magnitudes. Note that for the exponential case the mean albedo variation is almost constant up to 40% burned grid-cell, suggesting that fire induced albedo variation is only significantly detected if about half of the grid-cell area burns.
- The sigmoid (logistic) function (f_4) represents albedo change insensitivity for small and large burned events, concentrating most of the albedo decrease variation around the 50% burned threshold.
- The quadratic function (f_5), consisting in a parabola where the mean albedo variation increases for the small fire events but eventually starts to decrease for the larger fire events. This can represent small fire events over grasslands during the dry season, where the grass over the unburned part of grid-cell continues to dry out resulting in an increase in the albedo.
- The sinusoidal step-like function (f_6), representing smaller albedo variations throughout all fire event magnitudes with no apparent trend.

Table B.3

Mann-Kendall trend test result statistics for six types of simulated mean albedo variations by fire class magnitude. Test is applied using equally spaced pair values of 5% in burned area.

Function	Shape type	M-K score	p-val
f_1	Linear	-190	0.0
f_2	Exponential	-190	0.0
f_3	Logarithmic	-190	0.0
f_4	S-curve	-190	0.0
f_5	Parabola	-160	0.0
f_6	Oscillation	-22	0.96

Using 20 equally sized bins 5% intervals in burned area, the Mann-Kendall trend scores for the simulated relations shows that failure to detect a significant negative trend only occurs with the step-type sinusoidal (Table B.3).

All types of relations between albedo and burned area variation are consistent with condition (3) and lead to the detection of a significant negative trend. This is also observed in the cases where albedo might initially be constant or increase, as long as it eventually starts to decrease for the high magnitudes fire events. In the last case (f_6), although a negative trend is detected, it is not significant. Inverting this function would produce the same result but with a positive trend. These results show that the method for evaluating the coherency in the mean albedo variations is flexible enough to allow different kinds of responses to the fire event magnitude as long as the events are coherent. An inconsistent relation between both

variables, e.g. when condition (3) is not fulfilled, results in non-significance or even in a positive trend.

References

- Adams, J., Gobron, N., Mio, C., 2016. A study of land surface albedo conversion formulas using three-dimensional canopy radiative transfer modeling. *IEEE Geosc. Remote Sens. Lett.* 13 (8), 1039–1043. <https://doi.org/10.1109/LGRS.2016.2535160>.
- Alonso-Canas, I., Chuvieco, E., 2015. Global burned area mapping from ENVISAT-MERIS and MODIS active fire data. *Remote Sens. Environ.* 163, 140–152. <https://doi.org/10.1016/j.rse.2015.03.011>.
- Biondini, M.E., Mielke Jr, P.W., Redente, E.F., 1991. Permutation techniques based on Euclidean analysis spaces: a new and powerful statistical method for ecological research. In: Feoli E., O.L. (Ed.), *Computer assisted vegetation analysis*. Springer, Dordrecht, pp. 221–240.
- Bojinski, S., Verstraete, M., Peterson, T.C., Richter, C., Simmons, A., Zemp, M., 2014. The concept of essential climate variables in support of climate research, applications, and policy. *Bull. Am. Meteorol. Soc.* 95 (9), 1431–1443. <https://doi.org/10.1175/BAMS-D-13-00047.1>.
- Boschetti, L., Roy, D., Justice, C., 2009. International global burned area satellite product validation protocol, Part I-production and standardization of validation reference data. In: *Technical Report. CEOS LPV* (Ed.).
- Boschetti, L., Stehman, S., Roy, D., 2016. A stratified random sampling design in space and time for regional to global scale burned area product validation. *Remote Sens. Environ.* 465–478. <https://doi.org/10.1016/j.rse.2016.09.016>.
- Bowman, D.M., Balch, J.K., Artaxo, P., Bond, W.J., Carlson, J.M., Cochrane, M.A., D'Antonio, C.M., DeFries, R.S., Doyle, J.C., Harrison, S.P., et al., 2009. Fire in the Earth system. *Science* 324 (5926), 481–484. <https://doi.org/10.1126/science.1163886>.
- Cade, B.S., Richards, J.D., 2005. User manual for BLOSSOM statistical software. US Geol. Surv. Open-File Rep. 1353, 124.
- Cappucci, F., Gobron, N., 2017. Benchmarking of essential climate variables: Gamma index theory and results for surface albedo and aerosol optical depth. *Remote Sens. Environ.* 203, 90–100. <https://doi.org/10.1016/j.rse.2017.06.004>.
- Cescatti, A., Marcolla, B., Vannan, S., Pan, J., Roman, M., Yang, X., Caias, P., Cook, R., Law, B., Matteucci, G., Migliavacca, M., Moors, E., Richardson, A., Seufert, G., Schaaf, C., 2012. Intercomparison of MODIS albedo retrievals and in situ measurements across the global FLUXNET network. *Remote Sens. Environ.* 323–334. <https://doi.org/10.1016/j.rse.2012.02.019>.
- Chen, Y.-M., Liang, S., Wang, J., Kim, H.-Y., Martonchik, J.V., 2008. Validation of MISR land surface broadband albedo. *Int. J. Remote Sens.* 29, 6971–6983. <https://doi.org/10.1080/01431160802199876>.
- Dee, D.P., Uppala, S.M., Simmons, A.J., Berrisford, P., Poli, P., Kobayashi, S., Andrae, U., Balmaseda, M.A., Balsamo, G., Bauer, P., Bechtold, P., Beljaars, A.C.M., van de Berg, L., Bidlot, J., Bormann, N., Delsol, C., Dragani, R., Fuentes, M., Geer, A.J., Haimberger, L., Healy, S.B., Hersbach, H., Hölm, E.V., Isaksen, L., Kallberg, P., Köhler, M., Matricardi, M., McNally, A.P., Monge-Sanz, B.M., Morcrette, J.-J., Park, B., Peubey, C., de Rosnay, P., Tavolato, C., Thépaut, J.-N., Vitart, F., 2011. The era interim reanalysis: configuration and performance of the data assimilation system. *Q. J. R. Meteorol. Soc.* 137 (656), 553–597. <https://doi.org/10.1002/qj.828>.
- Dice, L.R., 1945. Measures of the amount of ecological association between species. *Ecology* 26 (3), 297–302.
- Dickinson, R.E., 1983. Land surface processes and climate—surface albedos and energy balance. In: *Advances in Geophysics*. Elsevier, pp. 305–353. [https://doi.org/10.1016/s0065-2687\(08\)60176-4](https://doi.org/10.1016/s0065-2687(08)60176-4).
- Fleiss, J.L., Levin, B., Paik, M.C., 2013. *Statistical Methods for Rates and Proportions*. John Wiley & Sons.
- Forbes, A.D., 1995. Classification-algorithm evaluation: five performance measures based on confusion matrices. *J. Clin. Monit. Comput.* 11 (3), 189–206.
- GCOS, 2011. Systematic observation requirements for satellite-based data products for climate. Supplemental details to the satellite-based component of the Implementation Plan for Climate in support of the UNFCCC (2010 UPDATE). In: *Technical Report GCOS-154*. World Meteorological Organization.
- GCOS, 2016. The global observing system for climate: implementation needs. In: *Technical Report GCOS-200*. World Meteorological Organization.
- Giglio, L., Loboda, T., Roy, D.P., Quayle, B., Justice, C.O., 2009. An active-fire based burned area mapping algorithm for the MODIS sensor. *Remote Sens. Environ.* 113 (2), 408–420. <https://doi.org/10.1016/j.rse.2008.10.006>.
- Govaerts, Y., Pereira, J., Pinty, B., Mota, B., 2002. Impact of fires on surface albedo dynamics over the African continent. *J. Geophys. Res. Atmos.* 107 (D22). <https://doi.org/10.1029/2002JD002388>.
- Hagolle, O., Lobo, A., Maisongrande, P., Cabot, F., Duchemin, B., De Pereyra, A., 2005. Quality assessment and improvement of temporally composited products of remotely sensed imagery by combination of VEGETATION 1 and 2 images. *Remote Sens. Environ.* 94 (2), 172–186. <https://doi.org/10.1016/j.rse.2004.09.008>.
- Heil, A., Yue, C., Mouillot, F., Calude, P., Caias, P., Keiser W., J., 2016. *ESA CCI ECV Fire Disturbance: D.1.1 User requirement document, version 4.1*. In: *Technical Report. ESA Climate Change Initiative - Fire CCI - Phase 2*.
- Hollmann, R., Merchant, C.J., Saunders, R., Downy, C., Buchwitz, M., Cazenave, A., Chuvieco, E., Defourny, P., de Leeuw, G., Forsberg, R., Holzer-Popp, T., Paul, F., Sandven, S., Sathyendranath, S., van Roozendael, M., Wagner, W., 2013. The ESA climate change initiative: satellite data records for essential climate variables. *Bull. Am. Meteorol. Soc.* 94 (10), 1541–1552. <https://doi.org/10.1175/BAMS-D-11-00254.1>.
- Janssen, L.L., Vanderwel, F.J., 1994. Accuracy assessment of satellite derived land-cover data: a review. *Photogramm. Eng. Remote Sens. (U. S.)* 60 (4).
- Jin, Y., Roy, D.P., 2005. Fire-induced albedo change and its radiative forcing at the surface in northern Australia. *Geophys. Res. Lett.* 32 (13). <https://doi.org/10.1029/2005GL022822>.
- Liang, S., Wang, K., Zhang, X., Wild, M., 2010. Review on estimation of land surface radiation and energy budgets from ground measurement, remote sensing and model simulations. *IEEE J. Sel. Top. Appl. Earth Obs. Remote Sens.* 3 (3), 225–240. <https://doi.org/10.1109/jstARS.2010.2048556>.
- Loew, A., Bell, W., Brocca, L., Bulgin, C.E., Burdanowitz, J., Calbet, X., Donner, R.V., Ghent, D., Gruber, A., Kaminski, T., Kinzel, J., Klepp, C., Lambert, J.-C., Schaeppman-Strub, G., Schrder, M., Verhoest, T., 2017. Validation practices for satellite-based Earth observation data across communities. *Rev. Geophys.* 55 (3), 779–817. <https://doi.org/10.1002/2017RG000562>.
- López-Saldaña, G., Bistinas, I., Pereira, J., 2015. Global analysis of radiative forcing from fire-induced shortwave albedo change. *Biogeosciences* 12 (2), 557–565. <https://doi.org/10.5194/bg-12-557-2015>.
- Mann, H., 1945. Nonparametric tests against trend. *Econometrica* 13, 245–259.
- Merchant, C.J., Paul, F., Popp, T., Ablain, M., Bontemps, S., Defourny, P., Hollmann, R., Lavergne, T., Laeng, A., de Leeuw, G., Mittaz, J., Poulsen, C., Povey, A.C., Reuter, M., Sathyendranath, S., Sandven, S., Sofieva, V.F., Wagner, W., 2017. Uncertainty information in climate data records from Earth observation. *Earth Syst. Sci. Data* 9 (2), 511–527. <https://doi.org/10.5194/essd-9-511-2017>.
- Mielke, P.W., 1986. Non-metric statistical analyses: some metric alternatives. *J. Stat. Plan. Inference* 13, 377–387. [https://doi.org/10.1016/0378-3758\(86\)90147-3](https://doi.org/10.1016/0378-3758(86)90147-3).
- Mouillot, F., Schultz, M.G., Yue, C., Cadule, P., Tansey, K., Caias, P., Chuvieco, E., 2014. Ten years of global burned area products from spaceborne remote sensing. A review: analysis of user needs and recommendations for future developments. *Int. J. Appl. Earth Obs. Geoinf.* 26, 64–79. <https://doi.org/10.1016/j.jag.2013.05.014>.
- Muller, J.-P., López, G., Watson, G., Shane, N., Kennedy, T., Yuen, P., Lewis, P., Fischer, J., Guanter, L., Domench, C., et al., 2012. The ESA GLOBALBEDO project for mapping the Earth as land surface albedo for 15 years from European sensors. In: *Geophysical Research Abstracts*. vol. 13. pp. 10969.
- Padilla, M., Stehman, S.V., Chuvieco, E., 2014. Validation of the 2008 MODIS-MCD45 global burned area product using stratified random sampling. *Remote Sens. Environ.* 144, 187–196.
- Pinty, B., Taberner, M., Haemmerle, V.R., Paradise, S.R., Vermote, E.F., Verstraete, M.M., Gobron, N., Widlowski, J.-L., 2011. Global scale comparison of MISR and MODIS land surface albedos. *J. Climate* 24 (3), 732–749. <https://doi.org/10.1175/2010JCLI3709.1>.
- Pinty, B., Verstraete, M.M., Gobron, N., Roveda, F., Govaerts, Y., 2000. Do man-made fires affect Earth's surface reflectance at continental scales? *Eos Trans. Am. Geophys. Union* 81 (34), 381–389. <https://doi.org/10.1029/00EO00281>.
- Porter, D.F., Cassano, J.J., Serreze, M.C., Kindig, D.N., 2010. New estimates of the large-scale arctic atmospheric energy budget. *J. Geophys. Res.* 115 (D8). <https://doi.org/10.1029/2009jd012653>.
- Ramaswamy, V., Boucher, O., Haigh, J., Hauglustine, D., Haywood, J., Myhre, G., Nakajima, T., Shi, G., Solomon, S., 2001. Radiative forcing of climate change in "Climate Change 2001: The Scientific Basis. Contribution of Working Group I to the Third Assessment Report of the Intergovernmental Panel on Climate Change". In: *Technical Report*. Cambridge University Press, Cambridge, U.K. and New York, NY, USA.
- Roy, D., Jin, Y., Lewis, P., Justice, C., 2005. Prototyping a global algorithm for systematic fire-affected area mapping using MODIS time series data. *Remote Sens. Environ.* 97 (2), 137–162. <https://doi.org/10.1016/j.rse.2005.04.007>.
- Schaaf, C., Wang, Z., 2015. MCD43C3 MODIS/Terra + Aqua BRDF/Albedo Daily L3 Global 0.05Deg CMG V006. In: *Technical Report*. NASA EOSDIS Land Processes DAAC.
- Story, M., Congalton, R.G., 1986. Accuracy assessment - a user's perspective. *Photogramm. Eng. Remote Sens.* 52 (3), 397–399.
- Tansey, K., Grégoire, J.-M., Binaghi, E., Boschetti, L., Brivio, P.A., Ershov, D., Flasse, S., Fraser, R., Graetz, D., Maggi, M., Peduzzi, P., Pereira, J., Silva, J., Sousa, A., Stroppiana, D., 2004. A global inventory of burned areas at 1 km resolution for the year 2000 derived from spot vegetation data. *Clim. Chang.* 67 (2), 345–377. <https://doi.org/10.1007/s10584-004-2800-3>.
- Tansey, K., Grégoire, J.-M., Defourny, P., Leigh, R., Pekel, J.-F., Van Bogaert, E., Bartholomé, E., 2008. A new, global, multi-annual (2000–2007) burnt area product at 1 km resolution. *Geophys. Res. Lett.* 35 (1). <https://doi.org/10.1029/2007GL031567>.
- Trenberth, K.E., Fasullo, J.T., Kiehl, J., 2009. Earth's global energy budget. *Bull. Am. Meteorol. Soc.* 90 (3), 311–324. <https://doi.org/10.1175/2008BAMS2634.1>.
- Tsendbarz, N., de Bruin, S., Mora, B., Schouten, L., Herold, M., 2016. Comparative assessment of thematic accuracy of GLC maps for specific applications using existing reference data. *Int. J. Appl. Earth Obs. Geoinf.* 44, 124–135. <https://doi.org/10.1016/j.jag.2015.08.009>.
- UCL-Geomatics, 2014. *CCI-LC Product User Guide*. In: *Technical Report*. UCL-Geomatics, Louvain-la-Neuve, Belgium.
- Wang, Z., Schaaf, C.B., Strahler, A.H., Chopping, M.J., Romá, M.O., Shuai, Y., Woodcock, C.E., Hollinger, D.Y., Fitzjarrald, D.R., 2014. Evaluation of MODIS albedo product (MCD43A) over grassland, agriculture and forest surface types during dormant and snow-covered periods. *Remote Sens. Environ.* 140, 60–77. <https://doi.org/10.1016/j.rse.2013.08.025>.
- Ward, D.S., Kloster, S., Mahowald, N.M., Rogers, B.M., Randerson, J.T., Hess, P.G., 2012. The changing radiative forcing of fires: global model estimates for past, present and future. *Atmos. Chem. Phys.* 12 (22), 10857–10886. <https://doi.org/10.5194/acp-12-10857-2012>.